



ISIS Horizontal Beam Line Stray Magnetic Field Mapping and Compensation

Brandon Dos Remedios¹

TRIUMF

Abstract: This report contains work surrounding the mapping of cyclotron stray magnetic field and progress in magnetic compensation design work, for the ISIS horizontal section replacement at TRIUMF. The first is addressed by extrapolated maps of on beam axis stray magnetic field, created from on and off axis magnetic field measurements, over the length of the injection system horizontal section replacement. The second is addressed by multiple optimal compensation configuration geometries of passive mu-metal shielding, found by finite element analysis simulations, alongside two principles for good mu-metal shielding found in the simulation data.

¹ University of British Columbia, Science Co-op Student (Physics) from May 2021 - Aug 2021, supervised by Marco Marchetto and Suresh Saminathan. School email: brados99@student.ubc.ca

Contents

1	General Introduction	2
2	Stray Field Mapping	5
2.1	Introduction	5
2.2	Methods and Materials	6
2.3	Data and Observations	10
2.4	Uncertainty	14
2.5	Discussion	15
2.6	Axially Symmetric Confirmation Measurements	19
2.7	Suggestions	22
2.8	Conclusion	22
3	Compensation Configurations	24
3.1	Introduction	24
3.2	Methods and Materials	26
3.3	Compensation Configurations Descriptions	29
3.4	Data and Observations	36
3.5	Discussion	37
3.6	Configuration Physical Mock-up Measurements	40
3.7	Suggestions	42
3.8	Conclusion	43
4	General Conclusion	44
5	Appendix	46
5.1	Rough Inside and Outside Beam Measurements	46
5.2	Generic Mu-metal and Cryoperm Comparison	47
5.3	Compensation Configurations Varying Thickness Data	48
5.4	Optimal Configurations Reduced Radius to 7.006 cm for Real Fit	53
5.5	Chained Configuration	55
5.6	Directory and File Descriptions	56

1 General Introduction

At TRIUMF, the 520 MeV cyclotron requires sourcing of material to produce its output of high energy proton beams; this material source being a hydrogen anion beam procured by a system denominated as the ion source injection system (ISIS). ISIS, alongside its current and in development ion sources, consists of a large electrostatic beam injection line which can be subdivided into 2 primary divisions. These are the vertical section, which was recently replaced around 2012 after operating for 36 years¹, and the horizontal section, which currently requires replacement. The horizontal section was originally completed in 1974², and has been in use since then. From this, replacement of the section in the near future would be prudent to reduce future maintenance and ensure avoidance of any failure of the injection system, which can become more likely with extended use.

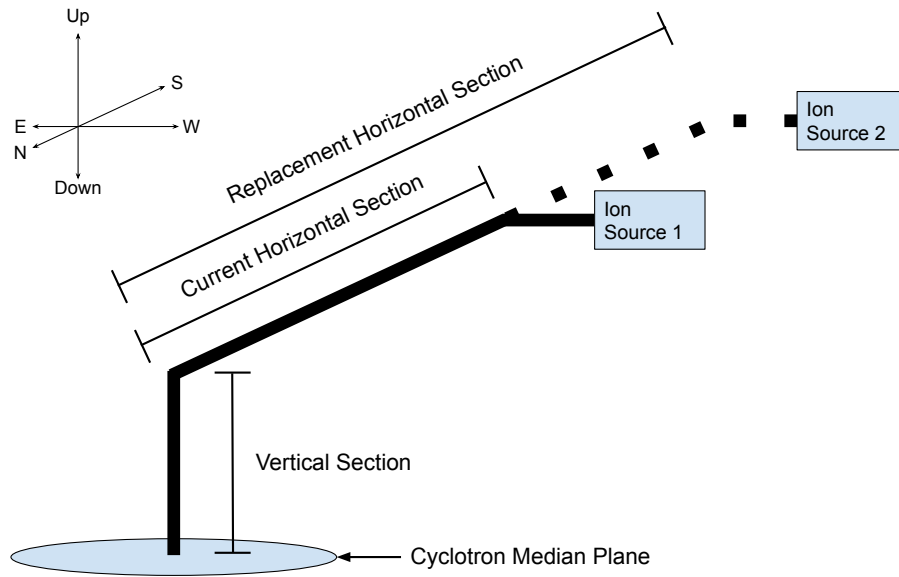


Figure 1: Isometric diagram showing relative position, to cyclotron median plane, of horizontal section, vertical section, and ion sources of ISIS.

The replacement to the original horizontal section will be similarly located at a height just above 13 m^3 vertically from the cyclotron median plane, leading into the top of the vertical section, and will stretch from the vertical section top to about 25.2 m away horizontally, placing it relatively proximal to the cyclotron. The cyclotron, being a massive magnet, produces a large stray magnetic field, and with the positional proximity of the replacement horizontal section to the cyclotron the hydrogen anion beam within the section will be effected by this field. Magnetic field compensation for the replacement horizontal section is thus necessary, to reduce the stray magnetic field's deflec-

tion of the anion beam. Stray magnetic field compensation for the horizontal section replacement, is the primary focus of this report.

Fortunately, from the Lorentz force law only 2 of the 3 components of stray magnetic field deflect the anion beam, and thus only 2 of the 3 were of real worry for compensation. These 2 components being the two transverse directions to the anion beam axis, which in this report are referred to as the vertical component (the magnetic field component in line with the vertical section of the injection line) and the horizontal transverse component (the magnetic field component perpendicular to the vertical component and the anion beam axis). The direction of the anion beam axis (the horizontal longitudinal direction), the direction of the vertical component, and the direction of the horizontal transverse component, form the rectangular coordinate system for this report, with the origin centered at the point of intersection between the vertical and horizontal sections' beams. The positive direction of the horizontal longitudinal axis points North to South, the positive direction of the vertical axis points down to up, and by necessity for a right hand ruled coordinate system the horizontal transverse direction points East to West.

There was a multitude of previous magnetic field compensation work in TRIUMF, that provided foundational knowledge for approaching the compensation problem in this report. To begin with, the original horizontal section also required compensation to deal with the cyclotron's stray magnetic field, and this compensation was done through a combination of soft steel shielding shells around the beam line, and an irregular assortment of small ferrite magnets⁴. The report⁴ on this gave a history of what was previously done, a starting point for passive compensation configurations, and also information for various features in the stray magnetic field mapping data. Further, much of the inspiration for the method of measuring stray field, comes from Arias in their report⁵ on stray field mapping for the ARIEL Electron Beam line. Finally, Baartman provides much of the initial background information for ISIS stray magnetic field compensation, a theoretical approximation of field expectation, which was useful in approaching the measurement process for the data of this report, and a proposal for active magnetic compensation in his report⁶.

Acknowledging those sources and building on them, this report addresses 2 primary topics regarding stray magnetic field compensation for ISIS' horizontal section replacement. First, the topic of finding the specific amount of stray magnetic field that must be compensated for, throughout the horizontal section. Second, the topic of finding a particularly advantageous compensation configuration, that can handle the amount of field found from the previous topic, especially in the most problematic area of the planned horizontal sec-

tion. This report is divided into two major sections each focusing on one of these topics. The Stray Field Mapping section seeks to address the first topic, by providing a mapping of the stray magnetic field along the horizontal section's beam axis. The Compensation Configurations section seeks to address the second topic, by providing principles for good mu-metal magnetic shielding configurations, found from simulations, and by providing optimal geometries for two general components of the replacement horizontal section.

2 Stray Field Mapping

2.1 Introduction

Knowing that the 520 MeV cyclotron produces a massive stray magnetic field and that the stray magnetic field encompasses the new horizontal section anion beam, it is clear that compensation for this magnetic field has to be designed for the new section, to reduce beam deflection. The first major step in designing this compensation, was measuring the magnitude of magnetic field to be compensated for, at all points along the anion beam axis, in each of the transverse directions to the anion beam axis (the vertical and horizontal transverse directions). This step of finding the amount of magnetic field was important, as it was necessary to know the magnetic field to ensure that the finalized compensation scheme would be enough to reduce field to an acceptable level and to prevent over compensation.

To find the magnitude of magnetic field along the beam axis, magnetic field was manually measured at various regular points along the anion beam axis, either on the axis or nearby the axis, when on-axis was not possible. These measurements were used to produce a final map of the magnetic field broken down into components of the 3 directions. Magnetic field had to be manually measured, as a purely theoretical approach or finite element analysis approach to the magnetic field mapping was simply not feasible, due to the cyclotron being extremely difficult to accurately model in either, and the many objects perturbing the stray magnetic field that could not be properly captured in either. Of these perturbing objects some of note, which likely had large effects in perturbing the stray magnetic field, are the steel rebar in the concrete between the cyclotron and the horizontal section, the steel of the beam frame supporting the current horizontal section, the steel of the various rails and flooring nearby, the steel of the current compensation scheme, the ferrite magnets of the current compensation scheme, and countless other proximal objects which all also effect the magnetic field by being magnetizable or by producing contamination magnetic field.

There were many challenges when attempting to produce the magnetic field measurements, especially surrounding the aforementioned perturbing objects, which resulted in necessary compromises in data collection when the jig assembly could not circumvent them. The most prominent of these challenges being the soft steel shielding shell of the current compensation scheme that surrounds the current horizontal section. This prevented any on beam axis measurements, for 18.9 m of the full 25.2 m horizontal beam length and introduced a necessity for extrapolating on-axis from data nearby the axis, further explained in the methods and materials and discussion subsections. Further,

due to various large diagnostic boxes and diagnostic devices along the beam length, the probe could not physically be placed to measure certain desired points, leading to a number of points along the beam axis having fewer extrapolation points to use, as shown in the data and observations subsection. Multiple other challenges of the measurement process were solved by the measurement jig and other tools, which are expanded upon within the methods and materials subsection.

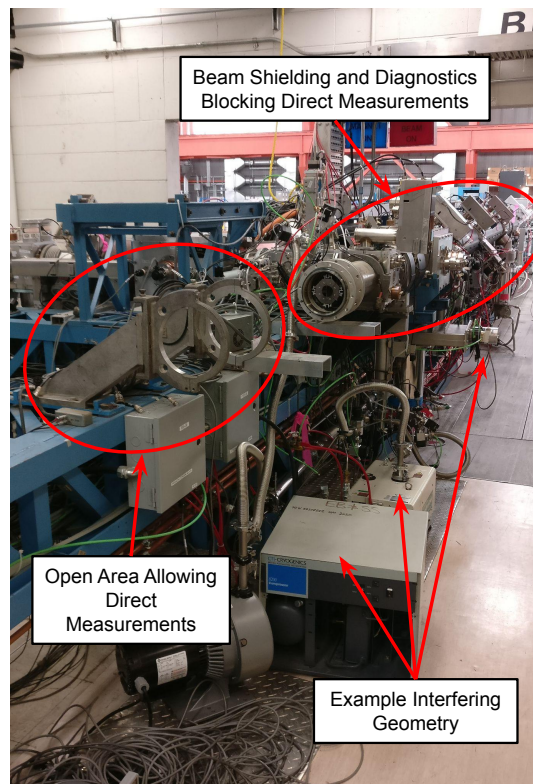


Figure 2: Picture showing the open area where direct measurements on-axis were possible, and the shielded area where direct measurements on-axis were not possible. Also displayed are examples of interfering geometry around the horizontal section, with geometry on the floor interfering with jig placement, and geometry above interfering with probe placement.

2.2 Methods and Materials

There were 3 primary tools used for the magnetic field measurements among various other smaller assisting tools. These 3 primary tools were the gauss meter, the laser tracker, and the custom tripod jig. The Lakeshore 460 Gaussmeter was used in conjunction with the Lakeshore MMZ-2512-UH 3-axis probe and the Lakeshore zero gauss chamber, to provide an accurate measure-

ment of magnetic field at each of the desired locations for the mapping. The Leica AT930 Absolute Laser Tracker, alongside multiple 0.5 inch and 1.5 inch spherically mounted retro-reflector (SMR) ball probes, and an iPod touch to display live measurements, provided accurate live measurements of location for the mapping process. Finally the custom tripod jig housing a 0.5 inch SMR ball probe near its center and the gauss meter 3-axis probe on its arm at a known and adjustable location from the ball probe, allowed the connection of accurate magnetic field measurement to that of accurate location measurement.

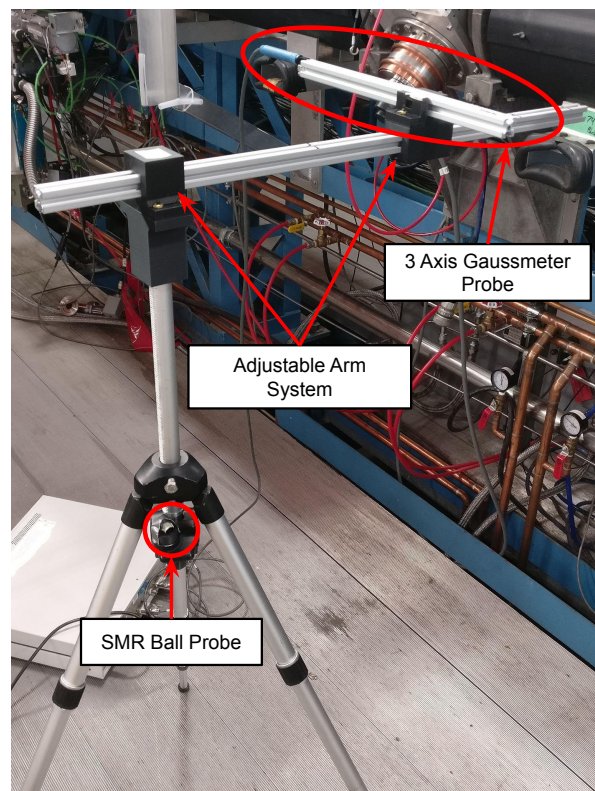


Figure 3: Tripod jig of experimental set-up for stray field mapping, including annotations for the laser tracker SMR ball probe placement, Gaussmeter 3-axis hall probe placement, and the adjustable arm.

Prior to the measurements the laser tracker was set up with an origin at the intersection point between the beam axes of the injection system's vertical section and the injection system's horizontal section. The coordinate axes were then set up expanding from this origin point, with one axis going along the hydrogen anion beam axis, one axis going vertically with gravity, and a final one orthogonal to the former two axes. These together with the laser tracker would allow one to view the absolute coordinates within the measurement

grid, of any given SMR ball probe. The tripod jig was also measured using measuring tape and previously known CAD dimensions of 3D printed parts, to find the displacement from the SMR ball probe's center, from its placement on a 3D printed mount on the jig, to that of the hall probe's center within the 3-axis probe, from its placement in the adjustable arm of the jig. On the adjustable arm of the tripod jig, lines were also measured and marked out with measuring tape ahead of measurements, to denote known adjustment points. This would allow one to do simple arm adjustments and with simple math, to know the adjustments' effect on displacement between the probes. With the arm allowing horizontal plane movement with these adjustments, this would allow for some flexibility in the placement of the base of the tripod jig, circumventing the difficult terrain below the beam line due to various devices and objects around it. Prior to measurements, the gauss meter was also set up running in the environment where measurements were to be taken, for at least 30 minutes as per manufacturer instructions⁷, so that the temperature of the gauss meter matched the environment.

With the various set-up done, right before the measurements the gauss meter and 3-axis probe were zeroed using the zero gauss chamber, and placed in the adjustable arm of the tripod jig. The 3 axis probe was locked in with another 3D printed part such that its roll was maintained within the arm, with its x-axis faced vertically and y-axis horizontally transverse. The 0.5 inch ball probe was mounted in its mount on the tripod jig, and the laser tracker set to measure that particular ball probe, reading its live position to the iPod touch.

For each measurement, the entire tripod jig was then moved to each desired measurement location, with each measurement location previously determined, such that the location read by the laser tracker would place the 3-axis gauss meter probe either directly on the axis of the anion beam, or a fixed displacement horizontally transverse from the anion beam at the same vertical height and same horizontal longitudinal displacement. The tripod's legs were adjusted as was necessary for terrain, with one or more legs being extended or retracted to avoid objects or account for diagonal ground, such that the ball probe and thus gauss meter probe would always be located in the desired spot. The tripod was placed such that the 3-axis probe's z-axis direction was coincident with that of the anion beam axis. At each measurement point, the front and back of the z-axis direction length of the 3 axis probe was measured, with measuring tape to local geometry, to ensure that the yaw was correct. Also, a level was placed on top of the adjustment arm along the two horizontal directions, to ensure that pitch and roll were correct, with the tripod legs being adjusted to fix any irregularities. With all of these, the hall probe of the 3-axis gauss meter probe would be correctly located at the desired spatial position, with alignment in pitch, yaw, and roll all regulated such that the probe would

correctly be aligned with the 3 directions, and thus be able to separately and accurately measure the 3 magnetic field components.

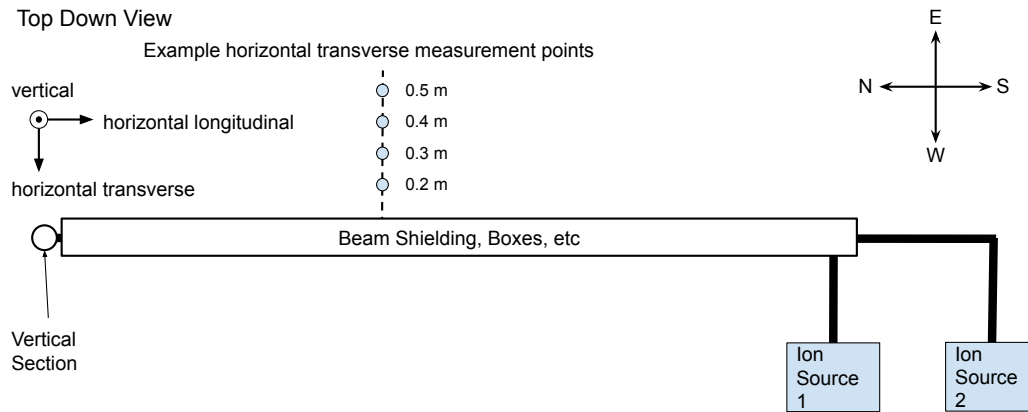


Figure 4: Visual aid showing top down view of the horizontal section with an example indirect measurement point, with markings of the 4 standard horizontally transverse points taken for the single horizontally longitudinal point.

At each desired spatial point the gauss meter was allowed time to settle such that fluctuations became small, and then the measurement of each of the 3 magnetic field components was recorded to 3 significant figures, truncating out much of the fluctuation. Measurements were taken every 0.3 m along the 25.2 m length resulting in 85 total points along the horizontal longitudinal direction of the anion beam axis. For points between 19.2 m and 25.2 m inclusive, there was no mild steel shielding or already existent anion beam, so the direct on-axis measurements were taken as the probe could be placed on the axis. For points between 0 m and 18.9 m, the mild steel shielding and anion beam prevented any on-axis measurements from occurring, so measurements were taken on one side of the anion beam axis at as many as was possible of 0.2 m, 0.3 m, 0.4 m, and 0.5 m horizontally transverse. The east side of the beam axis was the only side which could be used, as the west side had an interfering steel structure which would have forced any measurements to be far away and inaccurate due to the major steel structure's perturbation.

2.3 Data and Observations

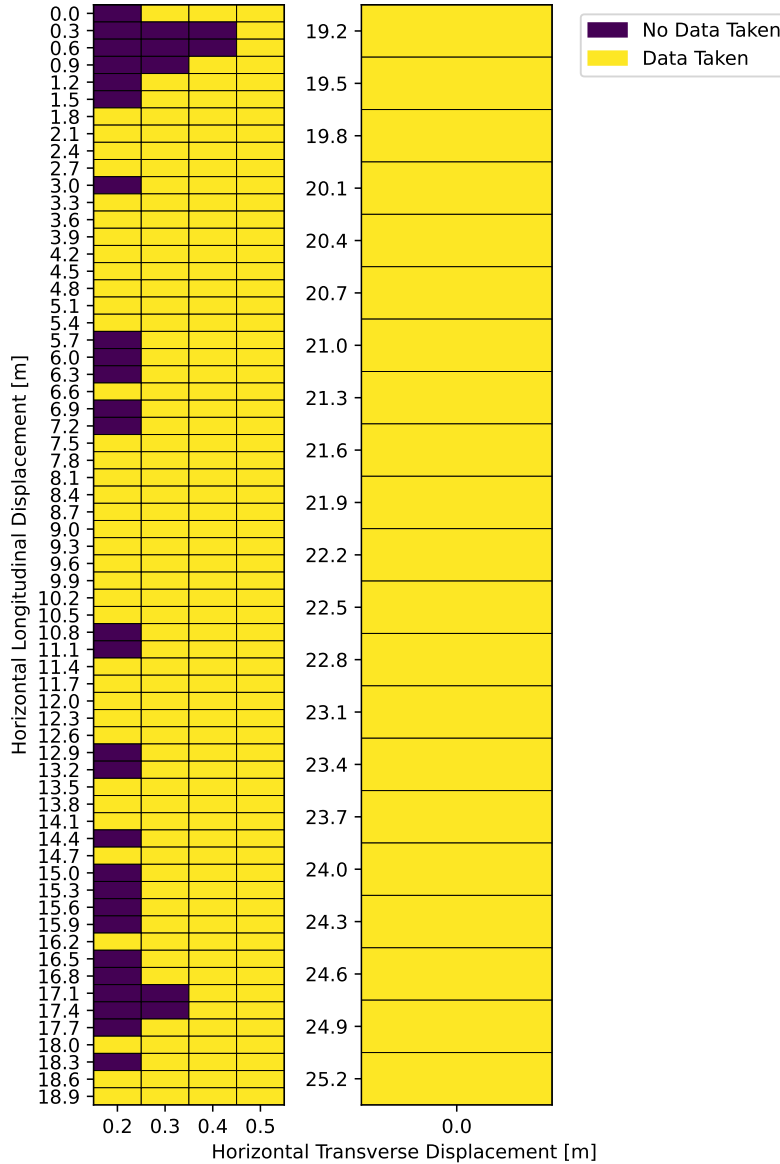


Figure 5: Data population plot showing locations where magnetic field measurements were taken.

The total data population is shown in figure 5, plotting all of the locations where the probe was able to be properly placed, and thus all the points where magnetic field measurements were taken. There was particular trouble with placement of the measurement set up at around 0.3 m away longitudinally, due to the hole in the ground where the injection system’s vertical section comes through, and at around 17.1 m away longitudinally, where the ion source 1

90 degree bend occurs. Various other locations longitudinally had diagnostics or other devices preventing the closest horizontally transverse measurement, at 0.2 m away, and those are also visible in the data population. Every measurement point longitudinally had the 0.5 m horizontally transverse point clear enough to be taken, and all points on-axis beyond 18.9 m were possible, meaning every planned point longitudinally had at least one measurement taken.

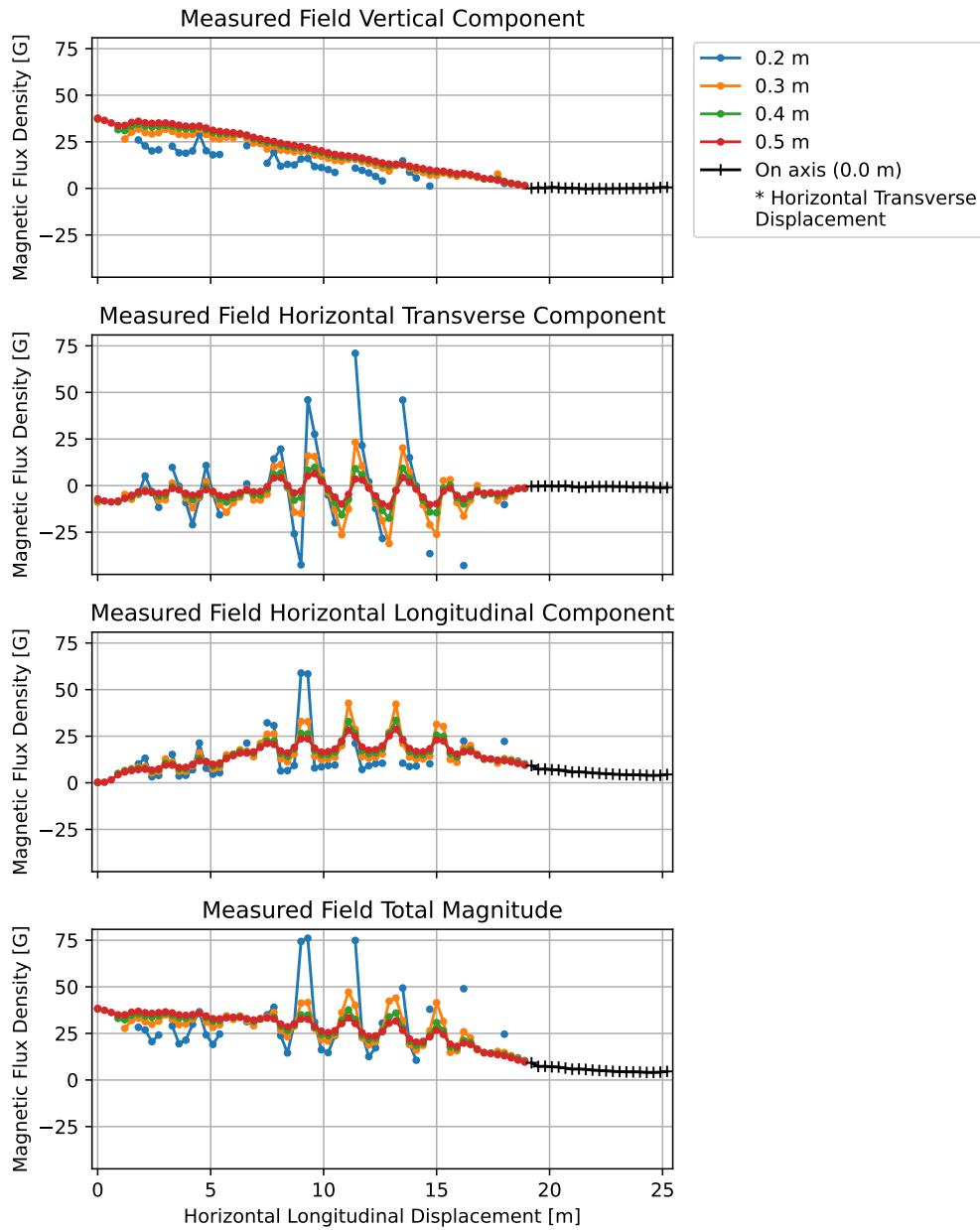


Figure 6: Field measurement data for direct on-axis measurements (0.0 m) and indirect horizontally transverse measurements (0.2 m, 0.3 m, 0.4 m, 0.5 m).

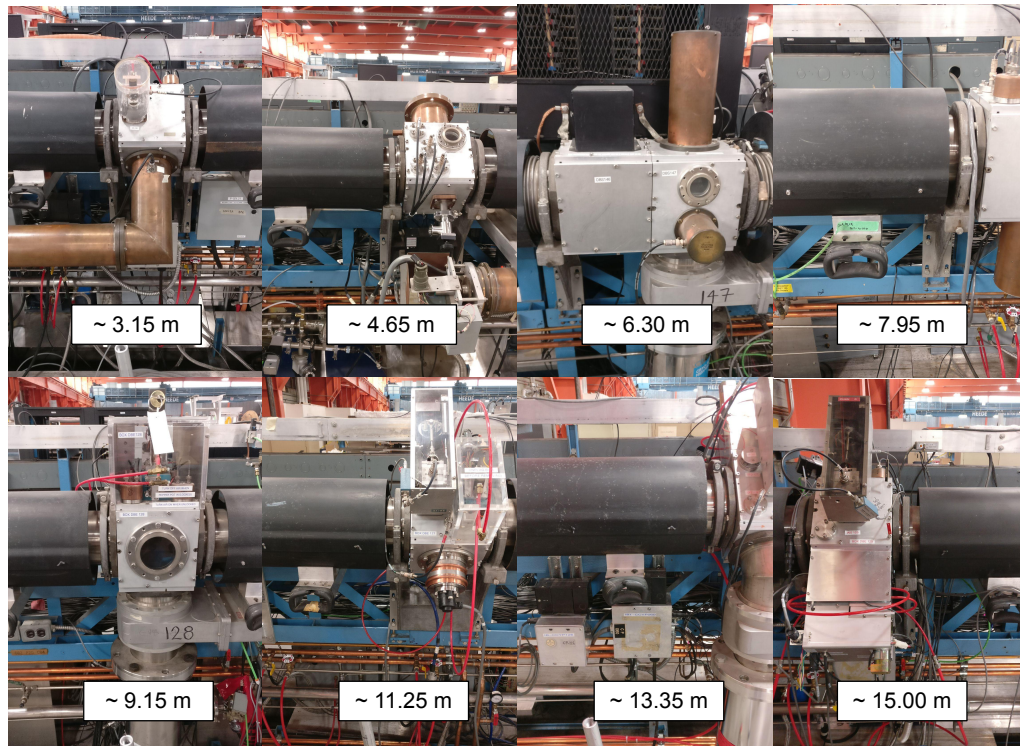


Figure 7: Current horizontal section pictures at around longitudinal displacements of field's horizontal component peaks. Peaks commonly occur at shielding edges.

The field measurement data for each of the locations in the data population are shown in figure 6. Observing the vertical component briefly, it can be seen that it behaves in a rather regular linear fashion, without many sharp changes in field or much disagreement between different horizontal transverse measurements at the same longitudinal displacement. Irregularities are more obvious in the two horizontal directions. There are multiple clear peaks in both, with larger ones commonly located at longitudinal displacements of around 3.15 m, 4.65 m, 6.3 m, 7.95 m, 9.15 m, 11.25 m, 13.35 m, and 15 m, which decrease in magnitude the further out horizontally transverse the measurement is. This likely means that the peaks are a contamination effect of the current horizontal section, possibly caused by the current compensation configuration's assortment of ferrite magnets, edge effects of the mild steel shielding, or a combination of both. This likelihood being from the horizontal transverse displacement decreasing the peak magnitude, which shows that it is likely a local effect of the current compensation. This point is further shown by pictures taken nearby these peak locations, shown in figure 7, where all peaks coincide with an end to the mild steel shielding, where ferrite magnets are located, and even more so this point can be shown by the lack of peaks in the axially symmetric confirmation measurements taken spatially away from the current compensation scheme, which are shown in a later subsection.

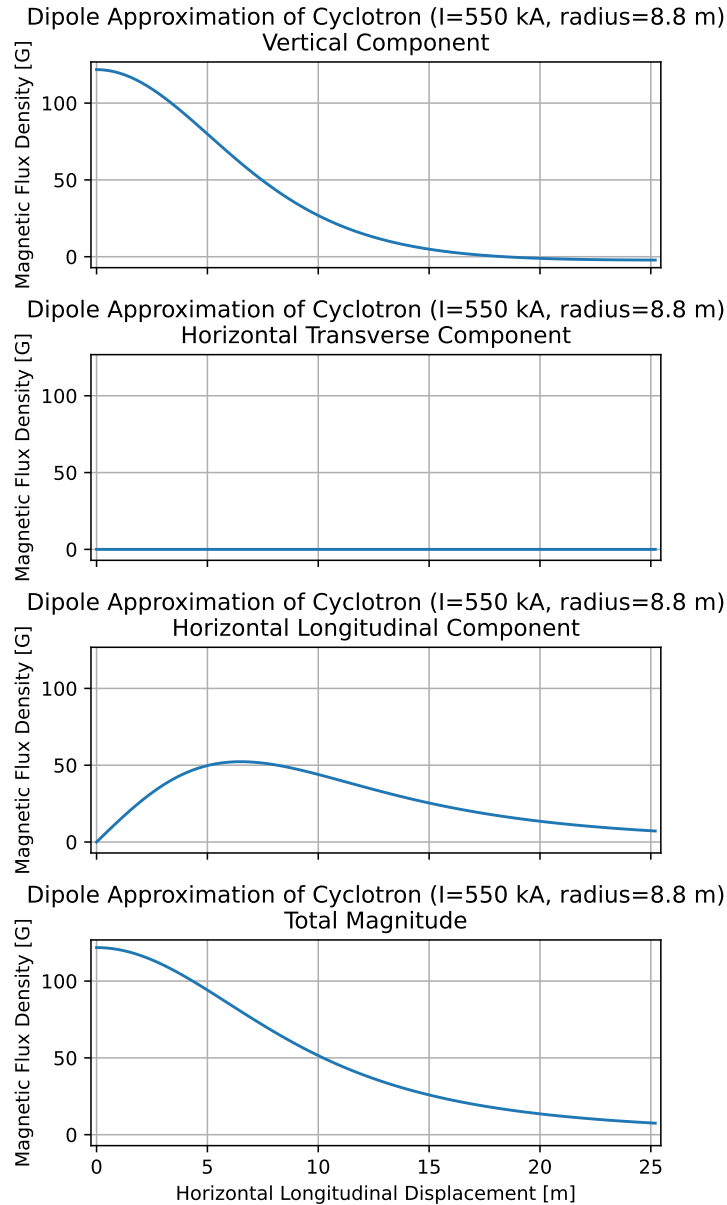


Figure 8: Theoretical expectation at height of 13 m, and along horizontal longitudinal displacement of 0 m to 25.2 m, of magnetic flux density of cyclotron, with cyclotron approximated as a 550 kA, 8.8 m radius magnetic dipole⁶.

Focusing on the general shape of the field measurement data, ignoring the local peaks, the general shape of the data seems to match the shape of the theoretical approximation expectation, as shown in figure 8, giving ground for confidence in the data. For the vertical component there is a maximum at the closest point to the origin, with a decrease towards 0 G as horizontal

longitudinal displacement increases, matching that of the expectation. The data has a more linear decrease than the more gaussian shape of the theoretical, which can be the effects of all the perturbing objects mentioned previously. For the horizontal transverse component the data remains consistently oscillating about around the 0 G line, matching that of the theoretical expectation, as due to axial symmetry there should be no horizontal transverse component. Finally, for the horizontal longitudinal component, the theoretical shows a rise, peak, and fall for this component, which can be clearly seen in the general shape of the measured data in the longitudinal direction.

2.4 Uncertainty

Speaking briefly on uncertainty in the measurements, the laser tracker has an advertised uncertainty of about $50 \mu\text{m}^8$ and the gauss meter has an uncertainty of about 0.1% of the reading⁷, with both of these instrument errors being negligible compared to the human measurement error for the spatial data, and fluctuation and truncation error for the field data. First addressing spatial uncertainty, the major uncertainty comes from the manual tape measures of the jig dimensions, from the SMR ball probe to the hall probe placement, and the acceptable range used when placing the tripod jig during the measurements, which was +/- 5 mm for each of the coordinate directions. For jig dimension measurements, each manual measurement had about 1 mm of uncertainty, with 2 trials made per measurement, and with 3D printed parts uncertainty from printer error being negligible in comparison. There were 4 manual measurements made for vertical displacement, 4 for horizontal transverse displacement, including the adjustable marks, and 2 for horizontal longitudinal displacement, including the adjustable marks. With the uncertainty from the acceptable tripod placement range propagated together with these, spatial uncertainty comes to +/- 5.2 mm for the vertical and horizontal transverse displacements, and +/- 5.1 mm for the horizontal longitudinal displacement. Addressing field uncertainty, due to the lack of need for high precision and the fluctuation of the reading of the gauss meter, measurements were taken to just 3 significant figures with fluctuations being limited to about a tenth of a gauss. This fluctuation range is the range used for uncertainty and is well over the manufacturer prescribed value mentioned earlier, so uncertainty in the field is +/- 0.1 G.

2.5 Discussion

With the multiple off-axis horizontally transverse measurements, from longitudinal displacement 0 m to 18.9 m, it was necessary to extrapolate from them to on-axis field, for a full map of magnetic field along the beam axis. From rough on-axis and off-axis measurements, around the open section between 19.2 m to 25.2 m, shown in appendix 5.1, it became clear that there was no best extrapolation method for extrapolating on-axis magnetic field, from off-axis measurements, as the off-axis measurements were not consistently correlating to that of the on-axis. To be clear, these extrapolation methods would need to take the available horizontal transverse measurements for a particular longitudinal point and extrapolate the value 0 m away transversely, which would be the on-axis field for that longitudinal point. Instead of a single best method, multiple extrapolation methods were trialed using the available data, and the best performing selected from them, with the criteria of finding the method which reduced local effects of peaks most, as from earlier those were shown to be result of the current “to be removed” compensation and thus are unwanted contamination in the data. Further, this selection criteria was made, as most extrapolation methods showed relatively similar results for extrapolated on-axis field, so the major advantage of any particular method would be ability to reduce contamination effect. Extrapolation methods and selection criteria are obviously quite crude and would most certainly lead to crude results for the on-axis field, however with the goal of mapping to be able to design compensation configurations within some safety factor, this was sufficient for the scope of this report. Refinement of the extrapolation methods and on-axis field results, is discussed in the suggestions subsection.

7 simple extrapolation methods were attempted for the extrapolation of on-axis field from the horizontally transverse points. 6 of these methods were really only 3 unique extrapolation methods, with 2 variants of each method based on the selection of horizontal transverse data used for extrapolation. These 3 unique methods were extrapolating the on-axis field as the mean of data, extrapolating the on-axis field as the max of data, and by extrapolating the on-axis field by a linear least squares fit. The first variant of each of these methods used all possible points of data for the extrapolation, and the second variant ignored the closest measurement of 0.2 m away transversely, but used all possible others. The mean and max simply ignored any missing data for their calculation, while the linear best fit did not run if the horizontal transverse data for the variant was not fully populated. Finally the last of the 7 methods simply used the furthest data point of 0.5 m away, as the extrapolated on-axis value. The results of extrapolated on-axis field, resulting from each of the 7 extrapolation methods. are shown in figure 9 alongside the direct on-axis measurements beyond 19.2 m.

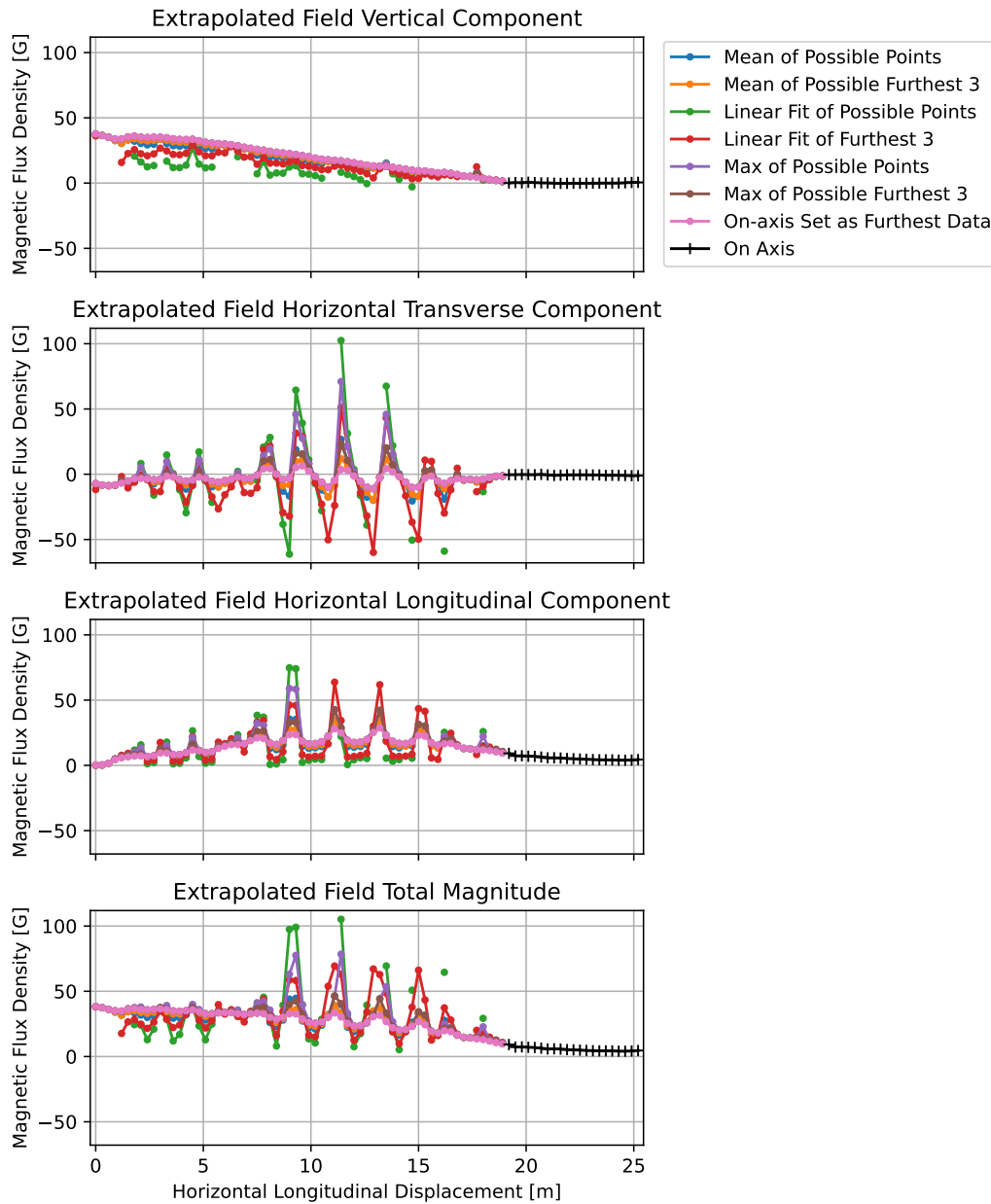


Figure 9: On-axis extrapolated field from 7 simple extrapolation methods, extrapolating on-axis field at each longitudinal point, using the horizontally transverse data taken at that point.

With the selection criteria mentioned previously, it became clear that any method including the 0.2 m away transverse point would exasperate the contamination peaks, so methods using all possible points were deselected in favour of those using the 3 further points. Further, linear best fit not only did not produce values for all longitudinal points, but also exasperated peak

magnitude relative to other methods, so those were deselected as well. Finally, as expected, the max value methods also did not suppress the local peaks due to them selecting the highest value, which was the peaks, so those too were deselected. This left the two methods of extrapolation of on-axis as the mean of the furthest possible three points, and extrapolation of on-axis as the furthest point's data, as the two best extrapolation methods for the selection criteria. These two are shown isolated with the on-axis measurements in figure 10.

Speaking briefly on the 2 best extrapolation methods, both reduce the effects of the contamination peaks most, and both have relatively matching shape to the earlier theoretical expectation. The mean method contains more data in its extrapolation than the furthest point method, and contains data closer to the extrapolation point than the furthest point data, meaning it likely has a lower error in it. Furthermore, this method is more sensible in a fashion due to it being a zeroth degree least square regression, and thus a common extrapolation method. For these reasons the mean method will be used as the mapping for the remainder of the report, being the mapping compared to the axially symmetric measurements, in the following subsection, and as the mapping of field used in the compensation configurations section. The furthest point method, while less robust and with more uncertainty, has the advantage of suppressing the local peaks the most, due to its further distance, and of having a consistent number of points used for each longitudinal point in its extrapolation process. While this report has more use for the mean method, the furthest point map may be useful in other contexts.

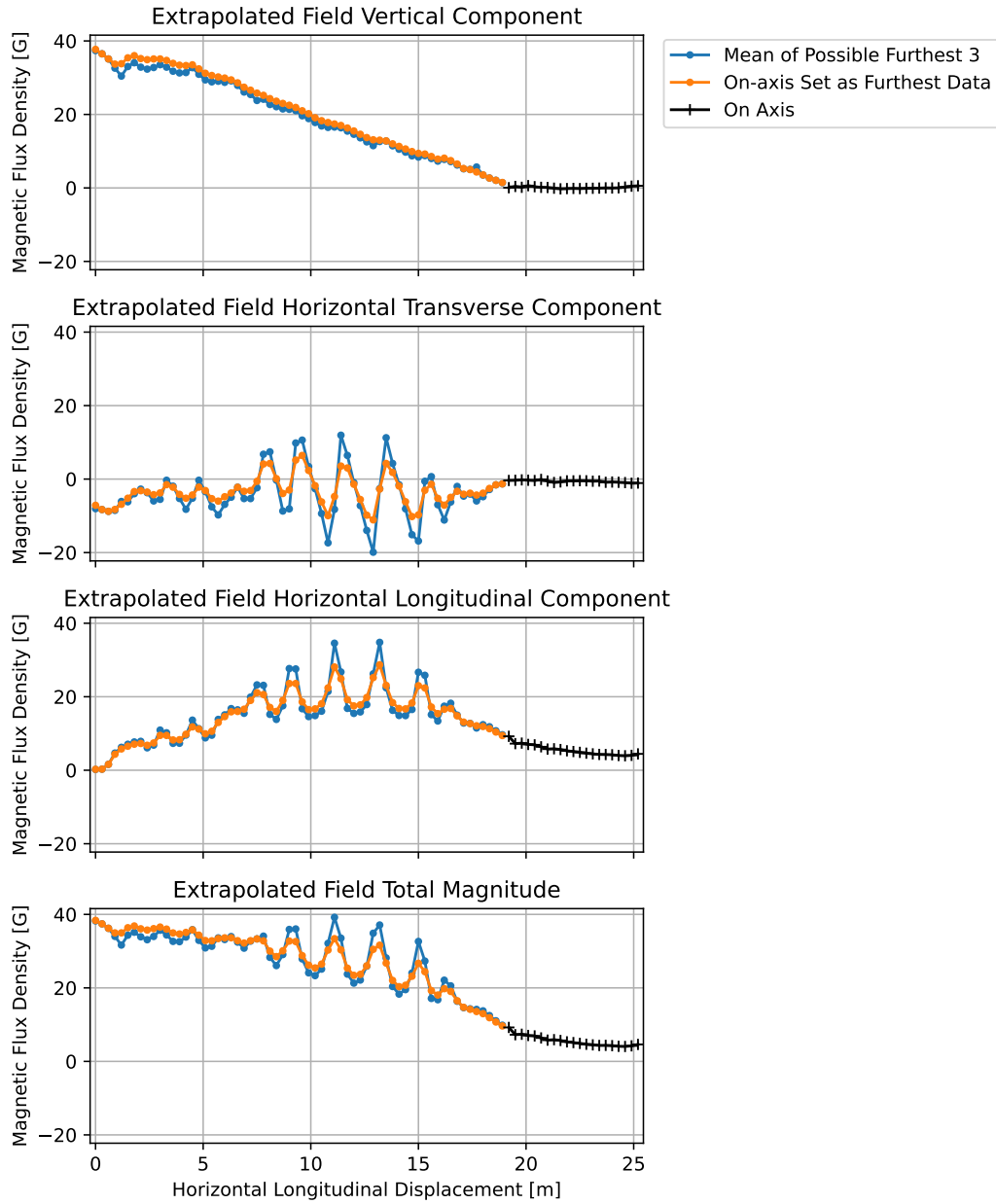


Figure 10: 2 best extrapolation methods based on selection criteria of reducing effects of contamination peaks.

2.6 Axially Symmetric Confirmation Measurements

The cyclotron, from the axial symmetry of its design, produces an axially symmetric magnetic field about the axis which is normal to the cyclotron plane. In theory, with no perturbations, one could measure radially outwards in any direction, at the same height of the beam axis, and obtain the exact same magnetic field measurements as would be recorded taking measurements directly on the beam axis. This would provide the on-axis measurements of magnetic field, without the necessity for extrapolation. However with perturbations and more importantly with the need to include perturbations in the mapping, as their effects need to be compensated for, the primary stray field mapping was not done in this fashion. This is because the measurements in any other radial direction, will not be able to include the effects of the steel beam frame, steel floor, and other local perturbing objects as other axial directions do not have this geometry. The axially symmetric confirmation measurements instead provide a good sanity check to the extrapolated stray field mapping, as extrapolated stray field despite perturbations, would likely not be wildly different from the axially symmetric measurements. Thus with the extrapolation not wildly differing from the axially symmetric measurements, there can be more confidence gained in the extrapolation map.

The measurement process for the axially symmetric measurements was similar to the process for the main stray field mapping measurements, mentioned in the Materials and Methods subsection. Measurements were taken at 110.5 degrees from the anion beam axis, which was simply the longest span of clearance to move the set up through. This span terminated with immovable interrupting geometry just prior to 3.6 m and just following 15 m radially outward, so the axially symmetric measurements were limited to between 3.6 m and 15 m inclusive, with measurements being taken every 0.3 m, similar to the main mapping. There were two major differences in the measurement set-up, which are displayed in figure 11. First, the tripod jig was not designed to go as high as was necessary to reach beam height from the lower axially symmetric path, so a non magnetic mobile platform was built to hold the tripod at the correct height for the measurement. Second, there was no local geometry to measure to, to ensure that yaw of the 3-axis probe was correct, as was done in the main mapping measurements. Instead a masking tape line was created along the measurement path using the laser tracker, prior to the axially symmetric measurements, and the yaw of the 3-axis probe regulated by alignment to this line using a string.

The axially symmetric measurements are displayed in figure 12. These measurements bear much resemblance to the theoretical expectation plotted in figure 8, with the vertical component having a similar gaussian shaped



Figure 11: Axially symmetric measurement experimental set-up of tripod jig and other tools on a mobile platform, and a tape alignment line on the ground.

decrease and a peak closer to the origin, the horizontal transverse component being constant and near zero, and the horizontal longitudinal component gradually rising, peaking, and falling off. Comparing the confirmation measurements to the stray field map, the stray field map seems to match the confirmation measurements general shape quite well, aside from the peaks of the stray field map. The axially symmetric measurements clearly do not have the peaks, further showing that the peaks in the stray field map are likely a local effect of the current compensation configuration. Disregarding the peaks, especially in the two horizontal components where they are most extreme, the general shape trend in the stray field mapping data seems to agree quite well with the confirmation measurements in terms of magnitude and shape. The two horizontal components' general trends, visually nearly

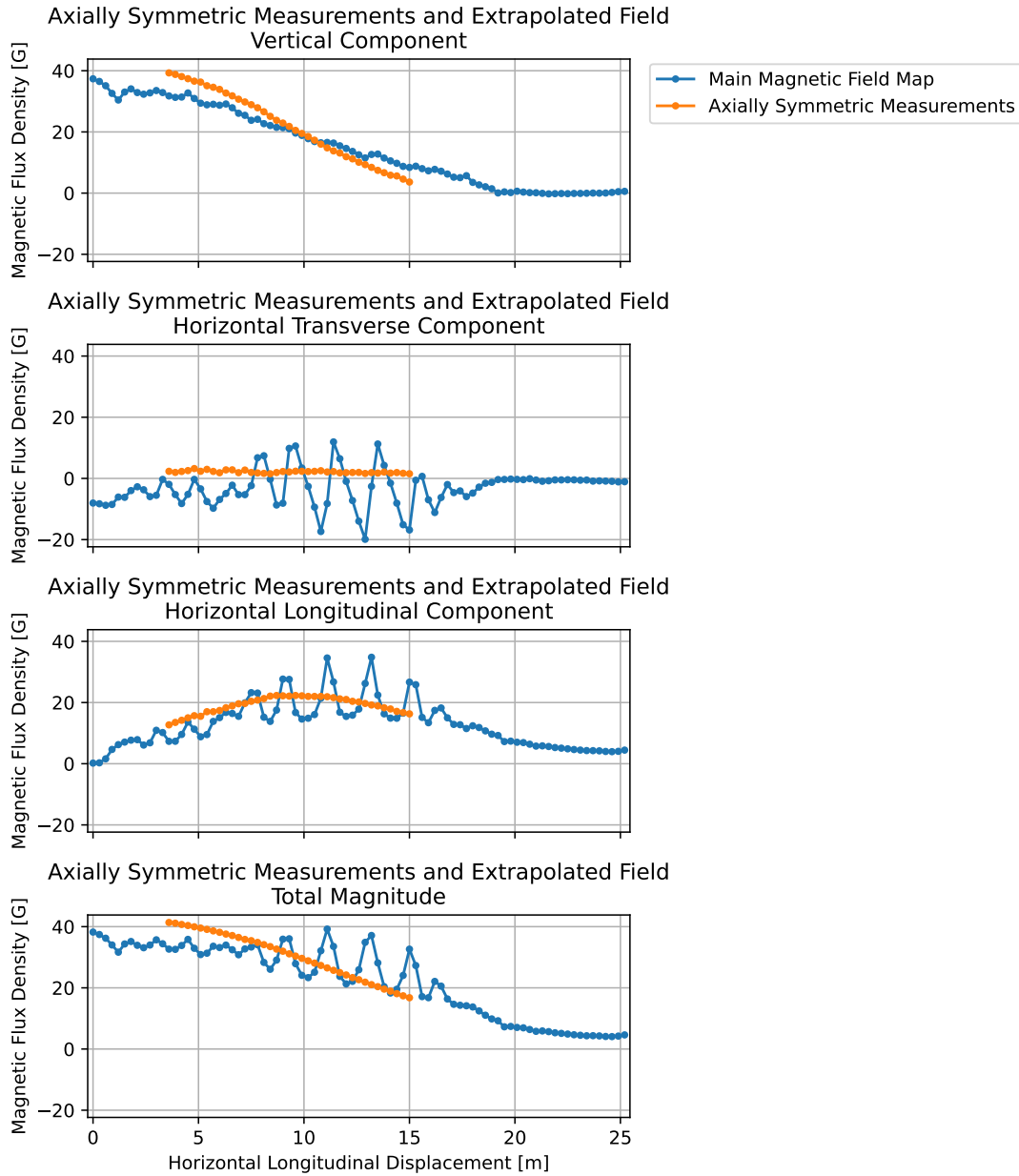


Figure 12: Axially symmetric confirmation measurements and magnetic stray field map, using mean of 3 furthest points extrapolation.

match exactly with the confirmation measurements. The vertical component seems to behave more linearly in the stray field map, than in the confirmation measurements, however that is likely due to the missing steel flooring beneath the confirmation measurements, which would have the greatest effect on the vertical component since the flooring is normal to it. Overall, with the general shape and magnitude of the stray field map seeming to match that of the

axially symmetric confirmation measurements, more confidence can be gained in the extrapolated map.

2.7 Suggestions

With the main overhead of jig manufacturing now completed it is recommended to perform multiple trials of the main measurements and the axially symmetric measurements, with the constructed jig, to reduce uncertainty in the data, especially removing uncertainty created from magnetic field fluctuations by averaging more measurements. Further, the extrapolation selection was rather crude, due to time constraints and lack of much data in the horizontal transverse direction for each longitudinal point. A good way to improve on that would be to take more horizontally transverse points for each longitudinal point, to have more data for an extrapolation of on-axis field, as well as using potentially more sophisticated and robust extrapolation methods compared to the relatively more simplistic ones used in this report. The localized contamination peaks seen in the stray field mapping also can be improved upon with future experimentation. One suggested option is to try using data smoothing methods to reduce the localized peaks and keep the important general trends in the components of the stray field map, which was not tried in this report simply for lack of expertise. Another suggested option is to take an exactly similar measurement map of the magnetic field, when the cyclotron magnet is off, and subtract that measurement from the current stray field map, this option being not attempted in this report from timing issues. With the magnet off, this measurement would only include the local effects of the current compensation scheme, and thus subtraction would superimpose the current compensation scheme's effects out of the stray field map. Finally with the axially symmetric confirmation measurements, time permitting it would be a good idea to confirm those measurements and find exactly the reason for the difference in the vertical component, which is speculated to be from the missing steel floor. To confirm the measurements, one can measure another radial direction and compare the data to the axially symmetric measurements seen here. To confirm ideas of the steel floor, it is suggested to model field in electromagnetic simulation software such as OPERA, with and without the steel floor, to see if the effects on field are similar, and thus prove or disprove the speculation.

2.8 Conclusion

Overall both extrapolation methods and their resulting extrapolations of on-axis measurements, shown in figure 10, sufficiently address the need to find the stray magnetic field to be compensated for. These two extrapolation

methods best suppress effects of current compensation in the data, and have encouraging resemblance to theoretical expectation. The mean map contains more data and is theoretically more robust, while the furthest point map is advantageous when consistency and suppression of current compensation scheme is most desired. The mean map, which will be used in the following section, is also confirmed by the axially symmetric measurements from similarity in shape and magnitude, when disregarding contamination from the current compensation scheme. This mean field map has maximal field magnitudes of 37.4 G in the vertical component, 19.9 G in the horizontal transverse component, and 34.8 G in the horizontal longitudinal component, which will be important in the following compensation configurations section.

3 Compensation Configurations

3.1 Introduction

Knowing the amount of magnetic field to compensate, from the stray magnetic field map, magnetic compensation configurations for the new replacement horizontal section, could be designed. These magnetic compensation configurations are the primary focus of this section. This section covers magnetic compensation proposals for two general components of the horizontal section replacement. The first general component, was any component sections of the replacement line with no radial openings, an example of which is seen in figure 13. The second and more interesting area of focus was compensation design for the standard diagnostic boxes of the new replacement beam line, pictured in figure 14. These diagnostic boxes had 4 large radial openings, diagonally oriented, and 8 smaller radial openings, vertically and horizontally oriented at the ends, created so that various diagnostics and devices could access the beam. These openings created a challenge, as they prevented a fully encasing compensation configuration, which was possible with the previous simpler no openings component, so more design work was necessary to make a configuration which could sufficiently reduce stray magnetic field on the beam axis. As an important note, compensation was designed to be internal to the two general components, as the geometry outside of the components is unknown.

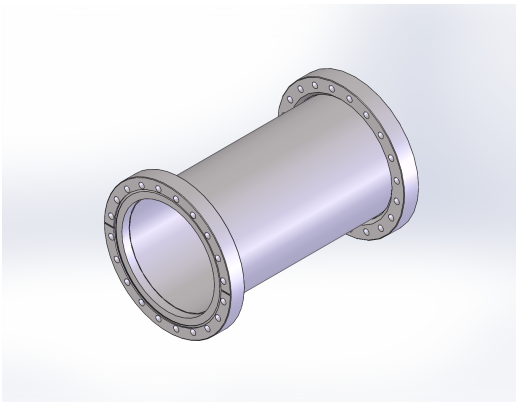


Figure 13: Example component of replacement horizontal section with no radial openings, assembly ART0014⁹.

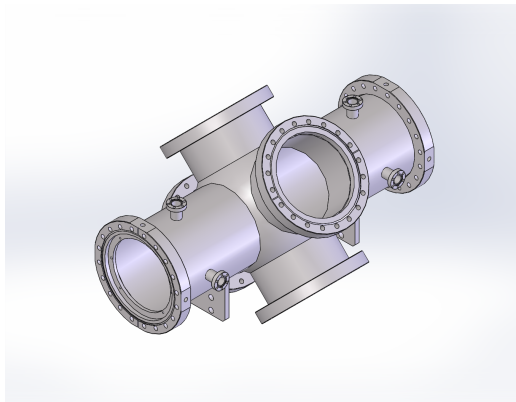


Figure 14: Standard diagnostic box for replacement horizontal section with multiple openings, assembly ART0204⁹.

In general, magnetic compensation can occur as either active cancellation or passive shielding. Active cancellation relies on creating an opposite and equal magnetic field, to cancel out the existing magnetic field, and will be discussed briefly in the discussion subsection. Passive magnetic shielding does not directly cancel the magnetic field, but instead redirects said field away from

an area, to create a volume of low magnetic field in the desired location. In this particular case, passive magnetic shielding will be the primary focus, with compensation configurations designed to redirect magnetic field away from the beam axis. This will reduce high magnitudes of transverse magnetic field there, such that the hydrogen anion beam is minimally deflected, with only transverse magnetic field reduction being of worry from the aforementioned Lorentz-Force law.

In designing passive magnetic shielding, there are multiple factors to consider to find the optimal configurations for the two general components. A good place to start is the selection criteria to use for selecting an optimal configuration. The major selection criteria for compensation is effectiveness of shielding, in this report simply meaning the amount of magnetic flux density in the transverse directions being left on-axis with the particular shielding configuration, with less field meaning a better configuration. The target for this report will be to reduce transverse stray field effects, on the beam axis, to under 1 G in magnitude, as that is a field magnitude commonly known at TRIUMF to be well within the correction capabilities of electrostatic steering. More specifically this will limit the horizontal transverse and vertical components individually to under $\sqrt{0.5}$ G each, which will keep the total field magnitude below 1 G. After the main consideration of shielding effectiveness, another piece of selection criteria is ease in construction, with more tangible lower complexity designs being more favourable.

With the criteria of shielding effectiveness and ease of construction, a design decision could be made regarding material for the passive magnetic shielding, before configuration comparisons began. Magnetic shielding uses a relatively high magnetic permeability metal to draw field away from the low field location, and is typically either low carbon steel or a nickel and iron alloy known as mu-metal. This relatively magnetically permeable metal eventually becomes saturated, when used to compensate too high magnitude of a magnetic field, meaning it is not able draw in anymore field lines and thus has an upper limit to the shielding it can provide. Low carbon steel, also known as mild steel, has a relatively lower permeability compared to mu-metal, meaning a necessity for thicker material, but also has a higher magnitude field requirement to saturate. Mu-metal has a very high magnetic permeability, meaning thinner material is usable, but saturates in lower magnitude fields than mild steel. This leads to mu-metal being advantageous in situations of low magnitude field shielding, and mild steel shielding advantageous in high magnitude field shielding.

From the stray field mapping it is known that the passive shielding will need to compensate for around 40 G which is well within the low magnitude field range of mu-metal. With mu-metal being able to achieve high shielding

effectiveness with more easily manipulable lower metal thicknesses, mu-metal is more favourable in terms of both selection criteria. Thus, this report will focus on the use of mu-metal, for the passive compensation of the two general components of the horizontal section replacement. This section outlines two principles of good mu-metal shielding configurations and provides baseline optimal geometries for compensation for the two general components.

3.2 Methods and Materials

The analysis for the mu-metal compensation configurations was done in the electromagnetic finite element analysis software suite OPERA. Specifically being done in OPERA-3D, which includes a 3 dimensional pre-process geometric modeller and post-process analyzer, with the TOSCA static field analysis algorithm being used for analysis. The experimental process consisted of the modelling and analysis of multiple different candidate compensation configurations, within a constant external magnetic field, with the middle symmetry axis of the configuration (the z axis for each of the geometric models) being the anion beam axis. The particular compensation configuration within the analysis would perform to shield the beam axis from the external magnetic field, succeeding to a differing degree for each configuration. Resulting on-axis field of the configuration and the configuration itself, was then compared against the others in terms of shielding effectiveness and ease of construction.

Constant Field Vertical Component	44.9 G
Constant Field Horizontal Transverse Component	23.9 G
Constant Field Horizontal Longitudinal Component	41.8 G

Table 1: Maximal values of stray field mapping, multiplied by safety factor 1.2. Component values are used as the constant external magnetic field in the analysis of compensation configurations.

The constant external magnetic field for the analysis of all configurations was chosen based on the concluding results of the stray field mapping section. To ensure that the configuration would work regardless of longitudinal displacement from the cyclotron, the maximal values of each component in the stray field map were used in field selection, which would also mean the likelihood of a safer overestimate. These maximal values were 37.4 G in the vertical component, 19.9 G in the horizontal transverse component, and 34.8 G in the horizontal longitudinal component. To further ensure that the selected compensation configuration would work in real life, an additional safety factor of 1.2 was applied to the maximal components. The resulting safety factored field, shown in table 1, was then used as the constant external magnetic field, applied in the magnetostatic analysis input in the pre-processor.

The analysis settings require input of magnetic field in oersted rather than magnetic flux density in gauss, however the conversion is simply 1 to 1 since relative permeability was almost 1, since stray field measurements were in air. The magnetic field horizontal longitudinal component was not of worry for shielding, but was included in the analysis in case its addition caused mu-metal magnetic field saturation. Also forcing of linear materials was used in the analysis for finding the most effective geometry, due to the number of simulations tested. This prevented results from completely matching real life data, but allowed for more time efficient work on iterations of configurations and still allowed for accurate relative comparisons of configurations to one another.

For each individual compensation configuration analysis, the configuration was first simply modelled geometrically, building the shielding geometry with mu-metal material, with the geometry spanning from -27 cm to 27 cm for length along the beam axis. The beam axis was the z axis for the configurations, with the y axis as the vertical direction, and the x axis as the horizontal transverse direction. This length of shielding would span the standard diagnostic box of figure 14 and was similarly used for the simpler no opening compensation scheme, for no radial opening general sections as in figure 13. The length was limited to 54 cm due to computational and time resources, as longer lengths would have reduced edge effects at the origin, where things were of interest, but also would have increased number of elements greatly, and thus strained both resources. This length was sufficient to accurately examine the effects of the configuration at openings at the origin, without having too much contamination from edge effects.

After this, the geometry was surrounded by large air cylinders, such that the analysis would have a large total potential volume to accurately converge by. The configuration was then surface and volume meshed, with the finite volume element mesh requiring the bodies of mu-metal to be meshed at a smaller maximal element size of 0.8, due to the thinness of the geometry, while generally elsewhere maximal element size was 2. There were two B-H curves available to define mu-metal material in the analysis, provided by a TRIUMF vendor Cryoperm. One was their Cryoperm metal and the other just of a generic mu-metal. Only the generic mu-metal was used for the majority of the compensation configurations, as the generic mu-metal curve and Cryoperm curve led to relatively similar results, as shown in appendix 5.2. Finally the meshed configuration was saved out into a database in CGS, and the TOSCA static field algorithm run to analyze the configuration.

After the analysis completed, the analyzed configuration was opened with the 3-D post processor, and a buffer generated of 1000 points along the beam

axis, from -27 cm to 27 cm. This buffer contained the data of magnetic field vertical component (column “RBY”) and magnetic field horizontal transverse component (column “RBX”) for each of the points on the beam axis, thus containing the performance of the compensation configuration in reducing on axis magnetic field. The buffer was then exported into a .csv file for data analysis, with the name containing the mu-metal thickness used for that particular analysis.

Regarding thickness of the geometry, metal thickness in the configuration was defined by a model dimension variable such that it could be easily varied, with each configuration being analyzed for multiple candidate thicknesses. For the simple no openings compensation configuration, metal thicknesses of 0.0508, 0.1016, 0.1524, 0.254, 0.5, and 1.0 mm were analyzed. For the diagnostic box configurations, testing was limited to the 3 thickest thicknesses at 0.254, 0.5, and 1.0 mm, since those were the only ones well below the target field for the simple fully closed compensation configuration, and it was assumed that radially opened configurations would perform much worse than the fully enclosed counterpart, so there was no point in analyzing 0.1524 mm or thinner. Not all configurations analyzed are displayed in the following subsections, since not all configurations had significant information brought forward by their analysis. In total 16 unique configurations were analyzed with the aforementioned process, with 13 of the 16 displayed and explained in the following subsection.

3.3 Compensation Configurations Descriptions

Simple Compensation: A. Solid Cylinder

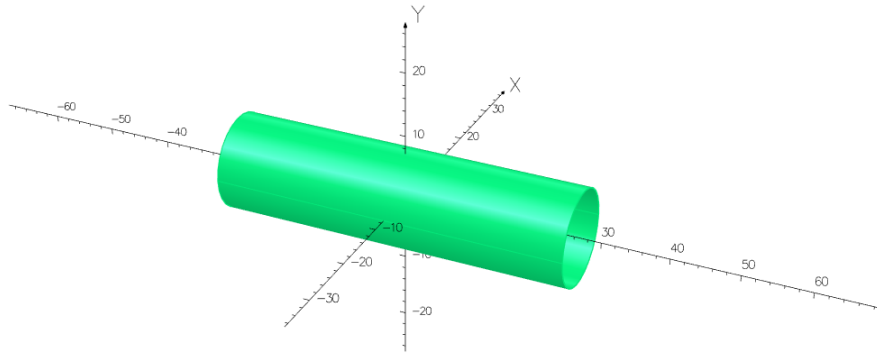


Figure 15: This compensation configuration is a simple solid cylinder of mu-metal and was meant to address shielding for any sections of the horizontal replacement with no radial openings. It is titled as serving these simple, no radial opening beam components, as opposed to those serving the more complex needs of the radial opening diagnostic box, as the other compensation configurations do.

Diagnostic Box: B. Gapped Middle Cylinder

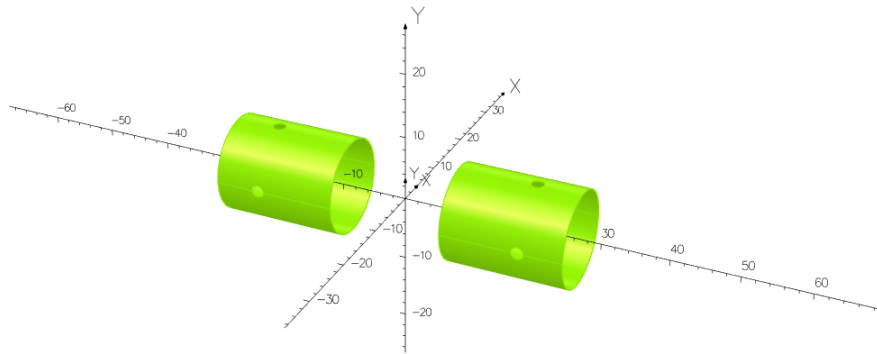


Figure 16: The gapped middle cylinder configuration is the simplest of those meant to shield the diagnostic box. It is the solid cylinder in figure 15 with a separation gap in the middle, allowing access for the large radial access openings seen in the middle of the diagnostic box in figure 14. It also has small vertical and horizontal holes punched in the mu-metal shielding near the ends, mirroring the smaller holes of the diagnostic box, and also featured in all following configurations.

Diagnostic Box: C. Full Cross

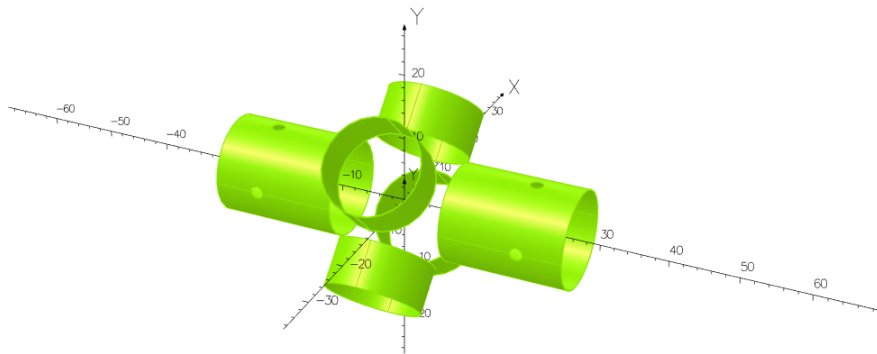


Figure 17: The full cross configuration introduces an additional set of 4 cylinders, arranged in a cross, which fit in the 4 diagonal radial opening tubes of the diagnostic box. This configuration extends the “full cross” cylinders just to the end of the cylindrical tubes, not extending them into the midsection of the diagnostic box.

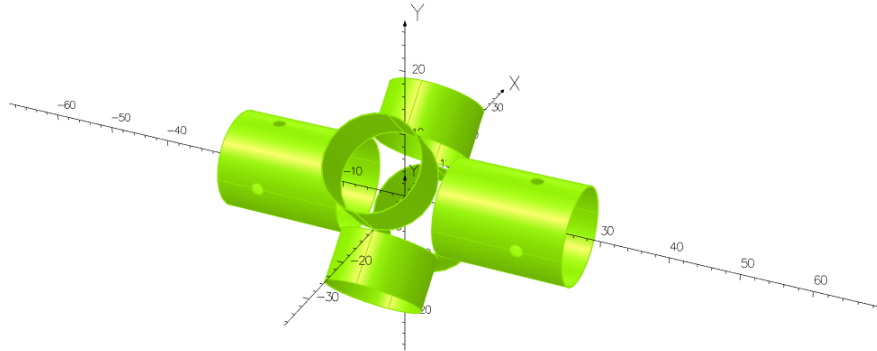
Diagnostic Box: D. Full Cross with Smaller Gaps

Figure 18: This configuration extends the full cross cylinders from figure 17 and the middle cylinder, into the middle section of the diagnostic box, shrinking the gaps between cylinders for more effective shielding. Specifically this configuration leaves just 2 mm of clearance length between the closest points of any 2 cylinders.

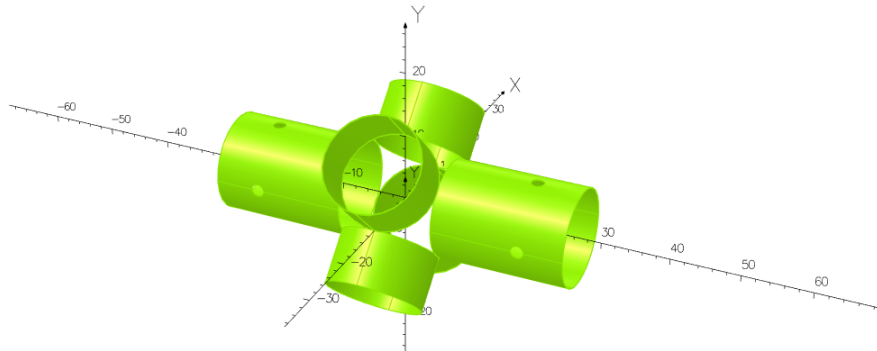
Diagnostic Box: E. Full Cross, Just Touching

Figure 19: Taking the shrunken gaps from figure 18 further, this configuration extends the cylinders such that each is in contact with the other, forming one continuous medium of mu-metal for magnetic flux density field lines to flow through.

Diagnostic Box: F. Full Cross with Connectors

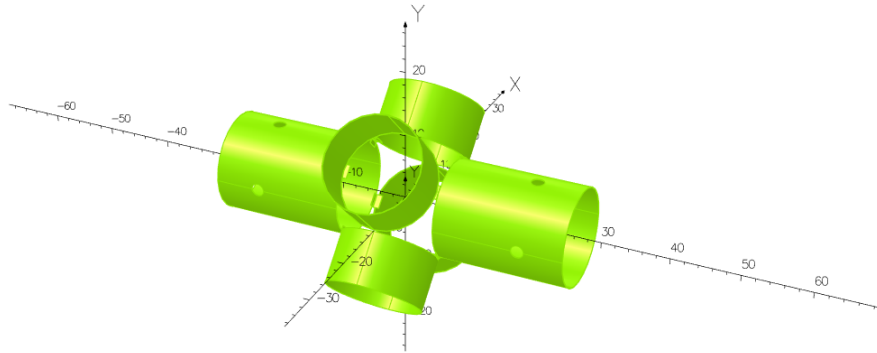


Figure 20: This configuration provides a similar continuous medium alike figure 19, but does so by introducing simple, more easy to work with, external corner connectors to the configuration of figure 18

Diagnostic Box: G. Continuous Middle Cylinder

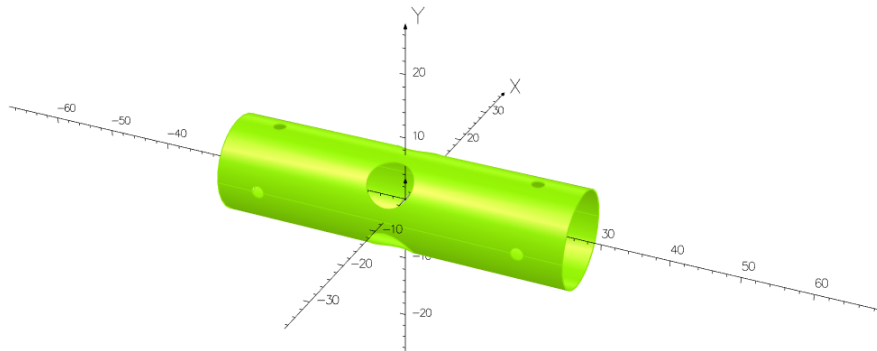


Figure 21: Instead of the complete separation gap introduced in figure 16, this takes the solid cylinder of figure 15 and introduces holes for the 4 diagonal openings of the diagnostic box, so that the configuration maintains a more continuous medium. These holes are not as wide as the radius of the diagnostic opening, to prevent a complete separation gap, and thus slightly cover the opening holes. They are 7 cm in diameter, which is enough for the 6 cm diameter requirement of the actual diagnostics being inserted, with a 1 cm clearance gap.

Diagnostic Box: H. Continuous Middle Cylinder with Full Cross

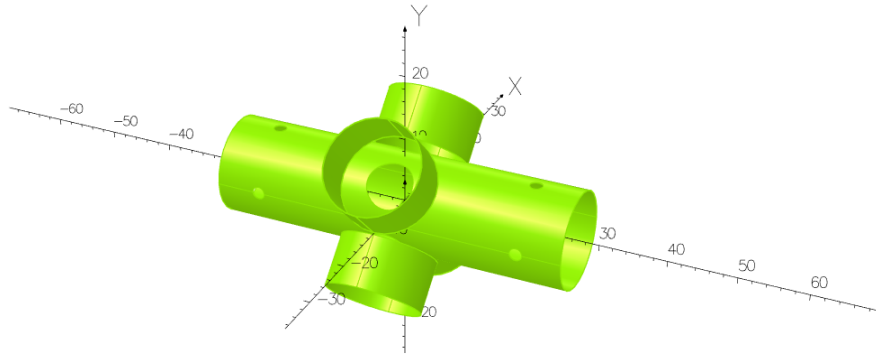


Figure 22: Building on the configuration of figure 21, this configuration adds the 4 full cross cylinders of figure 17, at 2 mm clearance spacing similar to figure 18, to improve shielding of the middle, diagonal, radial openings.

Diagnostic Box: I. Continuous Middle Cylinder with Full Cross and Connectors

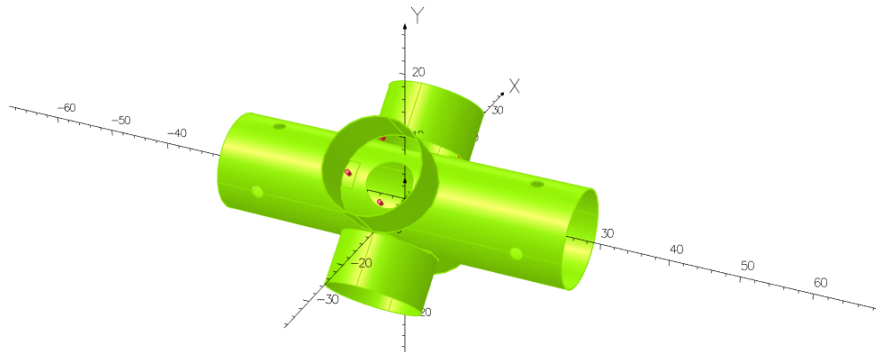


Figure 23: This configuration adds to that of figure 22, introducing easily constructable tabs to the full cross cylinders, attaching the full cross to the middle cylinder and creating a continuous medium of mu-metal. These tabs are simply secured by 1/4" steel bolts of 1" length. This configuration is one of the two optimal proposed configurations for shielding the diagnostic box.

Diagnostic Box: J. Tightly Contoured Continuous Middle Cylinder with Full Cross and Connectors

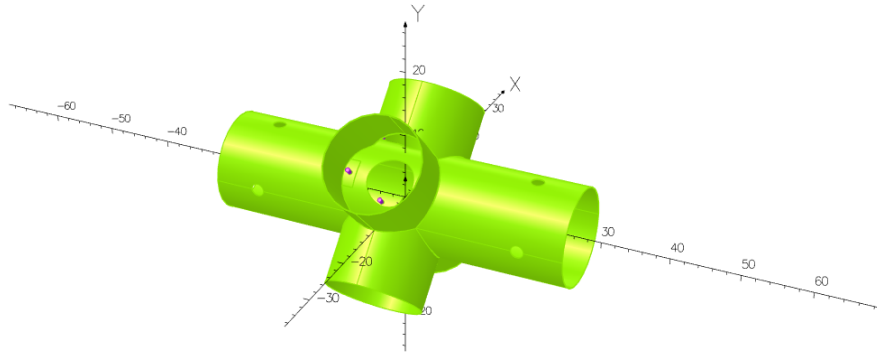


Figure 24: This configuration builds on that of figure 23, extending the full cross cylinders such that they are maximally contoured about all other cylinders, leaving minimal gaps. This is the second of the two optimal proposed configurations, for shielding the diagnostic box.

Diagnostic Box: K. Active Cancellation

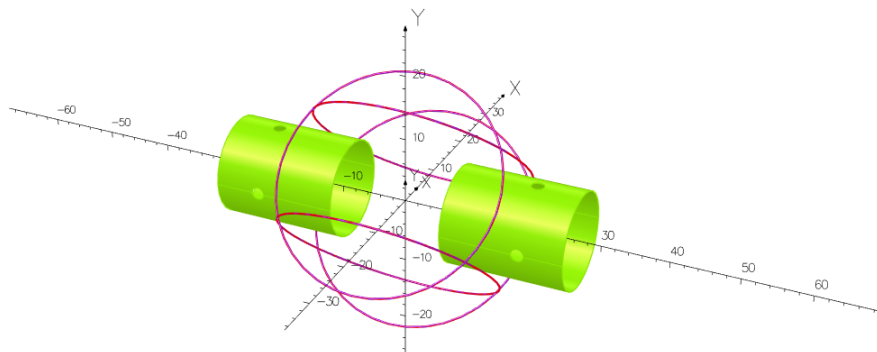


Figure 25: For some simple discussion of active cancellation, this configuration was included in this report. It uses the separated gap of figure 16, introducing active cancellation Helmholtz coils to deal with unwanted transverse field at the diagnostic box's middle openings.

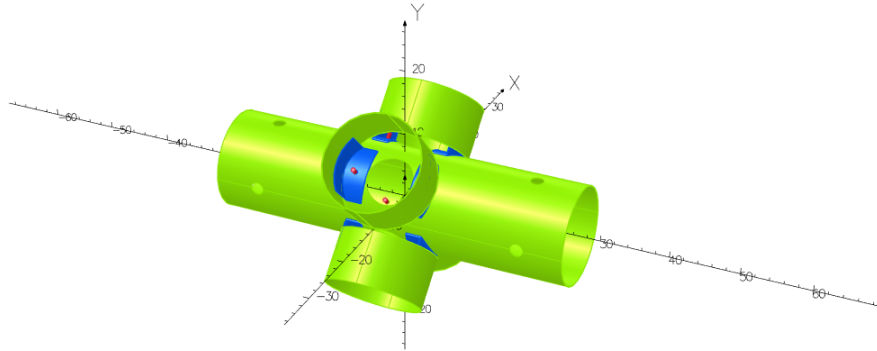
Diagnostic Box: L. Mild Steel Connectors

Figure 26: Instead of the connecting mu-metal tabs of figure 23, this configuration experiments with the effectiveness of separately constructed mild steel connectors, to create the continuous medium of the configuration.

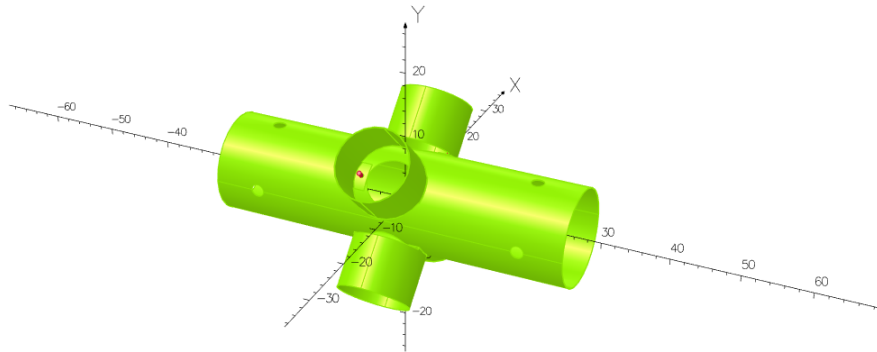
Diagnostic Box: M. Shrunken Aperture

Figure 27: A slight alteration to the compensation configuration of figure 23, this configuration experiments with the effects of a radius reduction in the 4 full cross cylinders.

3.4 Data and Observations

The data for transverse magnetic field on the beam axis, at 1 mm of metal thickness, for each of the configurations listed above, are plotted together for comparison in figure 28 and plotted with magnification in figure 29, with the full varying thickness data of each of the individual configurations plotted in appendix 5.3. Comparing just the 1 mm thickness for each of the configurations is good, as thicker metal always meant the same or better results for configurations, and 1 mm was the thickest thickness analyzed for all configurations. This meant that the best performance of each of the configurations was used, with the data comparisons and more being discussed in the following subsection.

As can be seen in figure 28, edge effects die off relatively quickly for each of the configurations, reaching near 0 G at around -20 cm to -15 cm, and symmetrically at 15 cm to 20 cm. These edge effects, outwardly beyond the near 0 G point, will be ignored for comparisons as in the replacement horizontal section, additional shielding components will be placed on either end of any instance of a configuration, removing any of these effects. Focus on comparisons will be placed on the single peak of the data for each of the diagnostic box configurations, seen at the origin, which is created by the middle radial openings of each configuration.

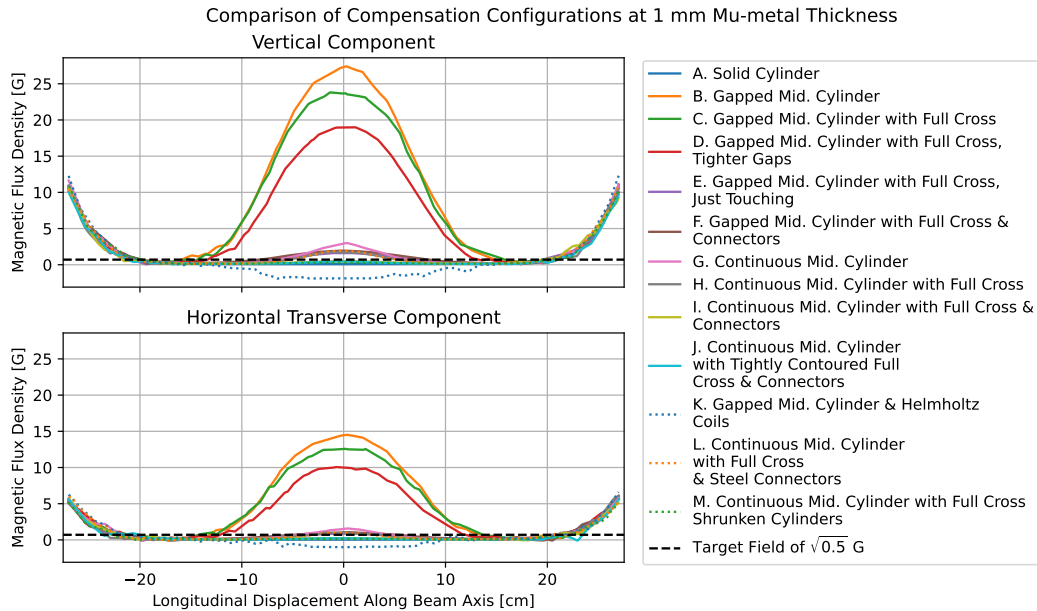


Figure 28: All compensation configurations' on-axis transverse magnetic field, at 1 mm metal thickness. The singular peak of comparison, which is required to be below the target field, is seen at the origin at 0 cm of longitudinal displacement.

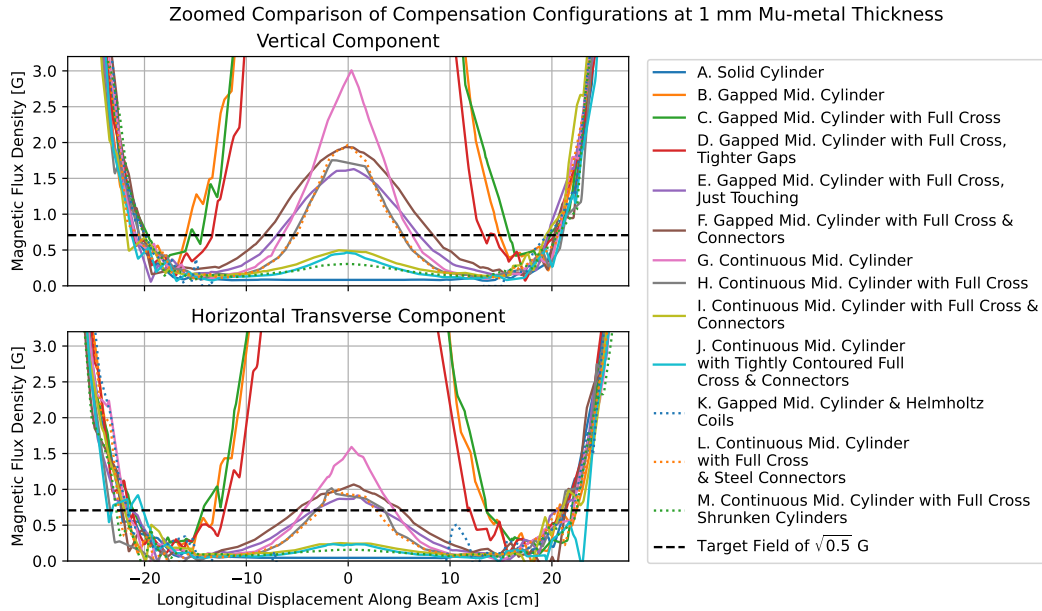


Figure 29: The same data as figure 28, with a magnified y-axis to see smaller magnetic field magnitude differences between configurations.

3.5 Discussion

Beginning with the simple compensation configuration of the solid cylinder in figure 15, as seen in the data of figure 29, the solid cylinder configuration both meets the target field requirement, of bringing field in the area of interest to below $\sqrt{5}$ G for each transverse direction, and outperforms all other radially opened compensation configurations analyzed, as expected. This simple cylinder of mu-metal will be the optimal configuration for any general component without radial openings.

Moving to the more complex diagnostic box shielding, the data from the variants of the full cross configuration (config C), seen in figure 17, show the first principle of designing good mu-metal shielding configurations. This principle is to have as large a continuous medium of mu-metal as possible for the configuration. This can be seen in the comparison of the data of the full cross with tight gaps configuration (config D) of figure 18 compared to the data of the just contacting, full cross configuration (config E) of figure 19, and also when compared to the data of the full cross with simple corner connectors configuration (config F) of figure 20. In the data, even with the very small 2 mm air gap of config D, the peak of magnetic field for the configuration is relatively massive in magnitude, peaking at around 18 G. As soon as the full cross cylinders are put in contact with the gapped middle cylinder in config E, creating the continuous medium of mu-metal, the effectiveness of shielding

improves drastically, with the peak shrinking to around 1.7 G. This effect can be also achieved by more easily constructable connectors of mu-metal in config F, which also has the peak drastically shrunk to around 2 G, with the simple connectors creating the continuous medium.

This continuous medium principle can be further seen in the comparison of the data peaks of the gapped middle cylinder configuration (config B) of figure 16 and the continuous middle cylinder configuration (config G) of figure 21, although not a perfect example like the previous comparison due to increased mu-metal in the former. This comparison more so shows the trade off between creating a configuration meeting the first principle, and the ease in construction for the design. With the configurations, achieving more shielding effectiveness by creating a more continuous mu-metal medium often created more complex shapes, such as config G which has a more complex cutout compared to the more simplistic config B. This is an often worthwhile trade-off, but just an important note to keep in mind for design. Also, this comparison shows that more mu-metal coverage of openings, leads to better shielding effectiveness, which is already obvious but shown in data here.

The second and last principle of good mu-metal shielding, put forward by this report, is shown in the comparison of the continuous middle cylinder configuration (config G) seen in figure 21 and the continuous middle cylinder with the 4 full cross cylinders configuration (config H) seen in figure 22, and also in the comparison of the gapped middle cylinder configuration (config B) in figure 16 and the gapped middle cylinder with the 4 full cross cylinders configuration (config C) in figure 17. This second principle is to have extra geometry nearby openings or problem areas, even if the geometry is not normal to the field lines it is trying to compensate for, to “catch” field lines straying into these areas and by this improve shielding effectiveness. In the data, this can be seen in the improvement of shielding effectiveness by the addition of the 4 full cross cylinders in either case, despite the cylinders not being connected to the middle cylinder (i.e. not fulfilling the first principle) and also not being planes of metal normal to the field lines entering into the openings. More specifically, in config G the peak occurs at 3 G, while the addition of extra geometry about the openings in config H drop the peak to under 2 G, and in config B, the peak occurs at around 27 G, which drops to around 24 G with the addition of extra geometry in config C.

Before reaching discussion of the optimal configurations for diagnostic box shielding, there are a couple brief miscellaneous points to be made about compensation configurations with configurations K and L. First, a brief note on active cancellation using the configuration with Helmholtz coils (config K) seen in figure 25. Active cancellation for the replacement horizontal section, may

not be the best compensation solution, due to the fact that over compensation is possible, as seen in the data of config K, with the overshoot to a negative transverse field. With this potential to overcompensate and thus deflect the beam in the other direction, one requires a very accurate map of the stray magnetic field to ensure this does not happen, and with the circumstances surrounding experimental mapping in the former section, this very accurate map may not be feasible. Second, mixed metal configurations in mild steel connectors were thought of and attempted in the analysis, to see if they were feasible due to lower cost and potential greater ease in overall construction. However, as seen in the data, mild steel connector configurations such as config L (displayed in figure 26) failed to reach the target field, even with maximal size of the connectors, and thus were discarded.

Finally reaching the optimal configurations, the first optimal configuration for diagnostic box compensation is the continuous middle cylinder with full cross cylinders and connectors (config J) displayed in figure 23. This configuration follows both of the aforementioned mu-metal shielding principles, with simple mu-metal tabs connecting the entire configuration into a continuous medium, fulfilling principle 1, and with the full cross cylinders “catching” field near the radial openings, fulfilling principle 2. With both of these principles fulfilled, it can be seen in the data of the configuration in figure 29 that the configuration manages to reduce the peak to under the target field line, despite the radial openings. The second optimal configuration is a more tightly contoured version of the previous configuration, providing more coverage over gaps and thus more effective shielding. This configuration (config J) is displayed in figure 24. In the data it can be seen that config J is slightly more effective at shielding than config I, which makes sense as it follows all of config I’s design, including following both shielding principles, just with additional shielding. This configuration comes with a trade off as with the better shielding effectiveness, it has more complexity and requires more difficulty in construction when compared to the previous configuration. Overall both fulfill the selection criteria of shielding effectively since both reduce the external field to the target. Further both are relatively easily constructable, with the first being more so, as the various cylinders can be simply cut out of sheets, rolled, and bolted together. Fulfilling both selection criteria, these are the best configurations for compensation of the diagnostic box.

As final notes on the optimal configurations, regarding them in the real horizontal replacement section, the real fit of the configuration in the real diagnostic box, will perform better than the data seen here, and additionally having two configurations in sequence leads to a relatively small field, despite small gaps. Addressing the first note, with the shielding fitting inside of the beam components, the radius of the cylinders could be reduced further, with

the reduction of the full cross cylinders for the first optimal configuration being analyzed in config M, seen in figure 27. As can be seen in the data, this reduction of radius leads to more effective shielding. This is key for the real construction of the configuration, as it will be placed in a vacuum chamber, so to avoid virtual leaks the radius of all cylinders will be reduced slightly compared to the analysis here. This will actually lead to more effective shielding in solving this problem, which can be seen in the data in appendix 5.4. Addressing the second note, in the real replacement horizontal section, multiple shielding configurations will be chained, as multiple general components (i.e. multiple simple non radially opened tubes or multiple diagnostic boxes) will be placed side by side. This is briefly studied in the data seen in appendix 5.5 and has promising results, but more study is encouraged as described in the suggestions subsection.

3.6 Configuration Physical Mock-up Measurements

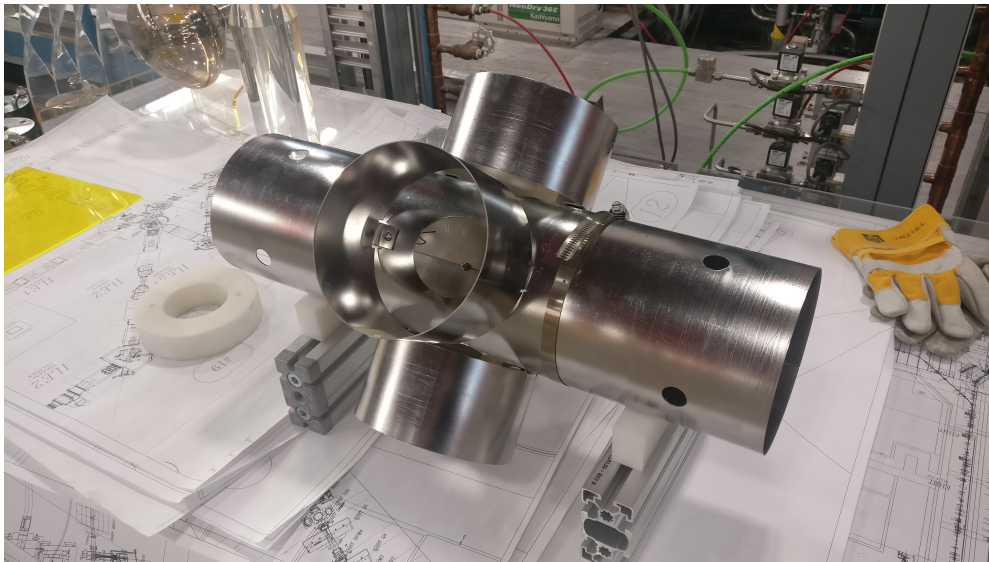


Figure 30: Physically constructed mu-metal mock up of configuration I, the configuration consisting of the continuous middle cylinder with 4 full cross cylinders and mu-metal tab connectors.

With the entirety of the compensations configuration work being completed in finite element analysis software, real measurement data to check the simulations' differences from reality was useful, especially before additional simulation work was done. For this real data, a mu-metal mock-up of the most easily constructable diagnostic box compensation configuration, configuration I, was created. This mock up is displayed in figure 30. The measurement procedure for the confirmation measurement data began with placing the mu-metal mock

up on a table nearby the vertical section of the injection system, where high vertical field was expected from the stray field map. A tape measure and the gauss meter from the stray field mapping data, were used for positional and magnetic field measurements. Using the tripod jig from the stray field mapping to maintain a constant origin position marking, the transverse magnetic field along the beam axis of the mock up shielding was measured, with measurements spanning 54 cm in length centered on the origin of the configuration, similar to the previous data of figure 28. Measurements were taken every 2 cm and also one off step at the origin. After the transverse magnetic field on axis within the mock up was measured, the mock up was removed and the same length measured again to get the uncompensated transverse magnetic field. With these measurements of real unshielded on-axis field, and real shielded on-axis field, the measurement of real shielding effectiveness for the optimal configuration, config I, could be examined.

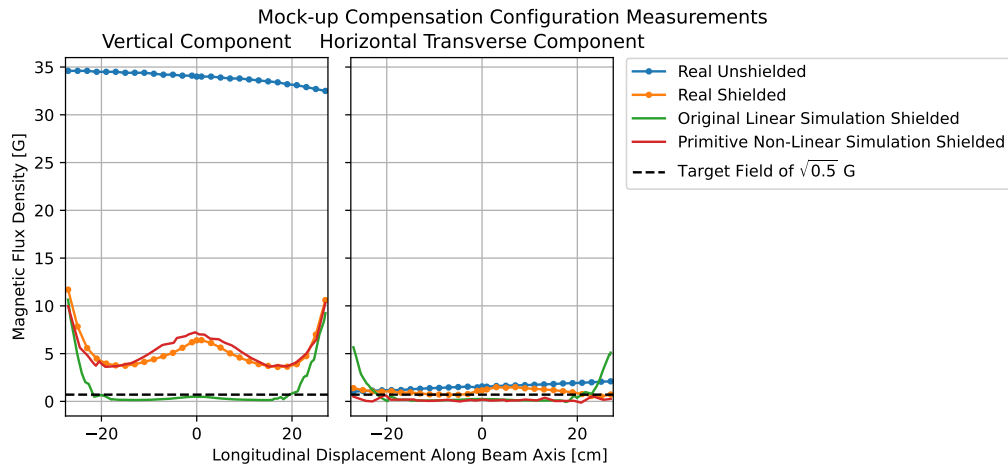


Figure 31: On-axis transverse magnetic field measurements of physically constructed mock-up. Includes measurements of background without the mock-up, measurements of shielded field with the mock-up, the original linear simulated expectation, and a primitive test of nonlinear simulated expectation.

In the physical measurements of figure 31 it is clear that the mu-metal mock-up reduces the magnetic field on-axis to a large degree, giving a good general sanity check for the configurations since they do reduce the on-axis field. However, there also is a large discrepancy between the amount of reduction in the field, with the real measured shielded field being much larger than the original simulated expectation, from the earlier simulations. This means that the real mock-up is much less effective at shielding than the simulation of it. This discrepancy is important as the reduced shielding effectiveness brings the field inside the shielding to above the target magnetic field, meaning the

field is no longer shielded to within electrostatic steering correction capabilities.

With the discrepancy in the mock-up measurements, multiple facets of the previous simulations may require additional work to better match reality. The main likelihood for the discrepancy is the linearity of the material used in the OPERA simulations, as the simulations in this report forced linear properties in material as mentioned in the methods and materials subsection. Although linear properties are sufficient in many cases, with the discrepancy, it may have been insufficient to represent the true resulting shielding effectiveness. This speculation is confirmed by primitive analysis of a non-linear version of the simulation, which matches the real mock-up measurements much more accurately. More thorough non-linear simulation analysis is encouraged in the following suggestions subsection. There are multiple other factors that may have also caused the mismatch, including overestimation of field, difference in mock-up geometry and simulated geometry, difference in material BH curves, and others. Further examination into both the simulations and the measurements, to uncover the reason for the differing data is highly encouraged.

3.7 Suggestions

The primary suggestion and future step for compensation configuration work primarily surrounds understanding the discrepancy between the simulations and the real mock-up measurements, explained in the previous subsection. Mainly, future experimentation re-examining the optimal configurations using the non-linear analysis setting in the magnetostatic analysis settings, is encouraged for confirming suspicions of the discrepancy. This examination remains uncompleted within this report due to time constraints. Further, exact modelling of the mock-up in OPERA and use of measured background field in the non-linear analysis is also encouraged, as these may provide closer results between the simulations and physical measurements. Once one manages to match the simulation to physical measurements, it may provide insight of the difference between the two, and with that knowledge of the difference additional work can be done to the current optimal geometries to increase shielding effectiveness to target field capability, in reality.

Beyond the discrepancy, the compensation configuration section of this report focused on a constant overestimate of the stray magnetic field, from the stray magnetic field mapping section. With forced material linearity potentially causing difference in field magnitude, simulation with more realistic field numbers is recommended. Since there is no well defined highest peak, multiple problem areas' field can be tested against the optimal configuration such as the field at the point of highest vertical component, or the field at

the point of highest overall magnitude. This is more feasible after the work of this section, as optimal geometry has already been selected, so many simulation iterations are unnecessary allowing for the longer non-linear analysis. Another suggestion for future experimentation is to test the configurations in non constant field, either by building an array of Helmholtz coils in OPERA to simulate one, or by using a different software suite that allows for it, such that the overestimates are not necessary. This may lead to lower cost and more easily constructable configurations for compensation. Some experimentation with non constant field analysis was completed, and the directory containing the experimentation is listed in appendix 5.6. Within either the constant field set-up or a non-constant field set-up, it is also encouraged to create a replica of the layout of the shielding for the horizontal sections, such that one can get a full axis map for the entirety of the horizontal section, containing any accumulation effects in field and the shielding effectiveness at all gaps. Primitive work on this is done with the comparison of two chained optimal configurations in appendix 5.5, but much more simulation work can be done, before the real horizontal replacement shielding is fully constructed.

3.8 Conclusion

In summary, progress for compensation for the two general components of the replacement horizontal section, has been made in the optimal configuration geometries discussed in this section. The solid cylinder configuration, config A shown in figure 15, addresses progress in compensation for simple, non radially opened components, by successfully reducing on-axis transverse field for them, within the report simulations, to the target requirement. The continuous middle cylinder with 4 full cross cylinders and connectors configuration, config I displayed in figure 23, and the more tightly contoured variant, config J displayed in figure 24, both address progress in compensation for diagnostic boxes, by being easily constructable and also by reducing on-axis transverse field to the required level, within the reports simulations; config J shielding slightly more effectively than config I, with the trade off of requiring more complex construction. These diagnostic box compensation configurations achieving their effective shielding by meeting the two principles of effective mu-metal shielding discussed in this report: First, that a configuration should be as large of a continuous medium of mu-metal as possible, and second, that a configuration should have extra geometry around required openings or problem areas. Finally, optimal configurations' simulations require more understanding of the discrepancy between simulation work and physical mock-up measurements, and future examination and experimentation for understanding this difference is highly encouraged.

4 General Conclusion

At the beginning of the report, two research topics regarding magnetic field compensation for the ISIS horizontal section replacement, were introduced: First, the topic of finding the magnitude of magnetic field to compensate, at various points for the replacement horizontal section's compensation scheme. Second, the topic of finding an optimal compensation configuration for the stray magnetic field found. With the measurements and mapping of the Stray Field Mapping section and the simulation work of the Compensation Configurations section respectively, progress on these two topics has been made.

Addressing the first topic, the two best extrapolations of the stray magnetic field measurements, which provide extrapolations of on-axis magnetic field over the length of the horizontal section, provide a satisfactory map of magnetic field magnitude, for the purposes of shielding design. These stray field maps, displayed in figure 10 both have particular advantages depending on context of use, with the method of the mean of the furthest points having less uncertainty, and the method of using the furthest data, having less contamination from the current horizontal section compensation scheme.

For the second topic, the optimal mu-metal shielding geometry of the solid cylinder of configuration A, displayed in figure 15, provides a satisfactory baseline optimal geometry for compensation for non-radially opened components of the horizontal section replacement, and the two optimal geometries of a continuous middle cylinder with 4 connected radial cylinders of configuration I, displayed in figure 23, and its more tightly contoured variant of configuration J, displayed in figure 24, provide satisfactory baseline optimal geometries for compensation for the diagnostic box of the horizontal section replacement. Both of these together, provide progress in creating an optimal compensation scheme for the whole horizontal section replacement, with the two principles of mu-metal shielding providing guides for further work in mu-metal shielding design. These two principles being, first to create as large a continuous medium of mu-metal shielding as possible, and second to have extra geometry around openings and problem areas,

Finally, with the magnetic stray field map, and the baseline optimal compensation configuration geometries, much more work for compensation for the horizontal section replacement can be completed, building upon them. It is primarily recommended in this report to refine the magnetic stray field mapping with additional data, and to understand more so the relation of compensation configuration simulation data with measured data, by additional simulation work, along with multiple other suggestions for future experimentation in each of the suggestions subsections.

References

- [1] TRIUMF, “Scientific activities report, 2010-2012,” (2012).
- [2] TRIUMF, “Annual report, 1974,” (1975).
- [3] R. Baartman in *XXXIX European Cyclotron Progress Meeting (ECPM), Ottignies-Louvain-la-Neuve, Belgium, 2015*.
- [4] R. Riches, “Magnetic Shielding and Permanent Magnet Compensation in ISIS,” Technical Report TRI-DN-76-5, TRIUMF, (1976).
- [5] G. Arias, “Ambient Magnetic Field Compensation for the ARIEL (Advanced Rare IsotopE Laboratory) Electron Beamline,” Technical Report TRI-BN-14-05, TRIUMF, (2014).
- [6] R. Baartman, “Magnetic field compensation for ISIS,” Technical Report TRI-BN-20-18, TRIUMF, (2020).
- [7] Lake Shore Cryotronics, [User’s Manual Model 460 3-Channel Gaussmeter](#) (Lake Shore Cryotronics, Ohio, 2017), pp. “2-5”.
- [8] Hexagon, “Hexagon_MI_Tracker_Absolute_Tracker_brochure_A4_en_WEB,” (2021).
- [9] M. Ilagan, “ART0014,” Internal Resource, TRIUMF, (2017).
- [10] M. Ilagan, “ART0204,” Internal Resource, TRIUMF, (2017).
- [11] M. Ilagan, “ART0268,” Internal Resource, TRIUMF, (2017).
- [12] M. Ilagan, “ART0052,” Internal Resource, TRIUMF, (2017).
- [13] K. Ahrends, S. Reyes, and T Gay, “Helmholtz spacing of thin rectangular magnetic field coils,” *Rev. Sci. Instrum.* **91**, 116103 (2020).

5 Appendix

5.1 Rough Inside and Outside Beam Measurements

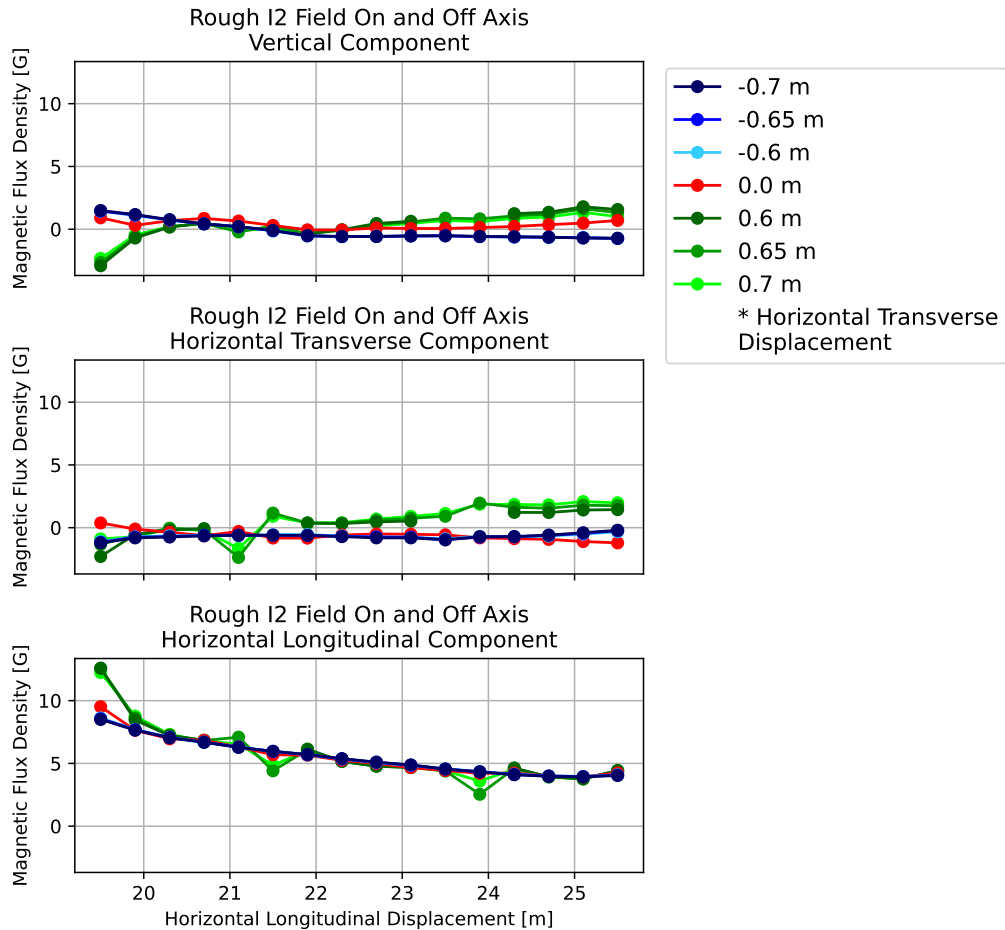


Figure 32: Rough measurements on-axis and off-axis at the open section of I2 North to South. As can be seen in the data, the East and West off-axis measurements do not consistently remain above or below the on-axis measurements, nor do they form any consistent linear relationship with the other measurements for a single longitudinal displacement point. This all makes a best method for extrapolation difficult to find.

5.2 Generic Mu-metal and Cryoperm Comparison

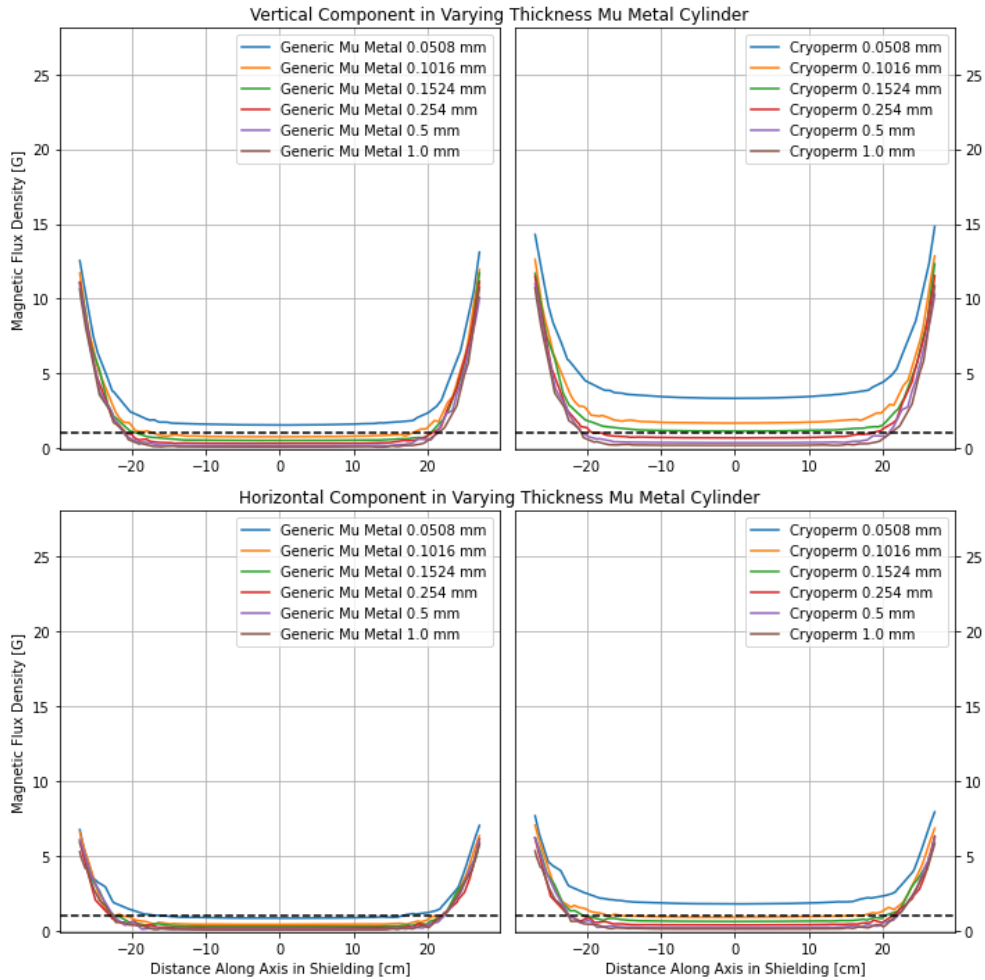
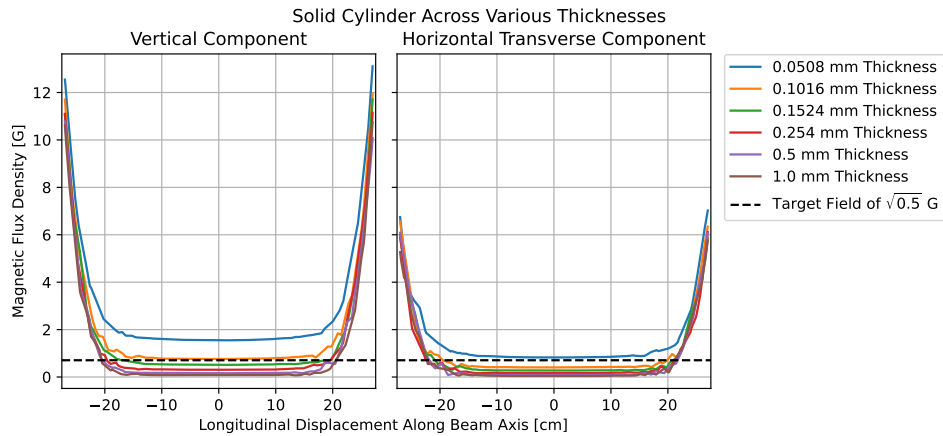


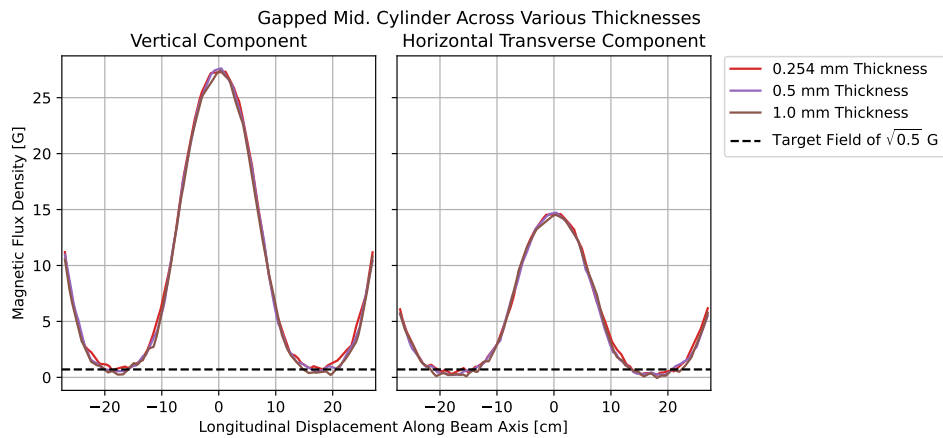
Figure 33: As can be seen in the comparison, CryoPerm shields slightly less effectively than the generic mu-metal, however the difference is very slight, with the difference shrinking to nearly nothing when approaching the larger metal thicknesses of interest.

5.3 Compensation Configurations Varying Thickness Data

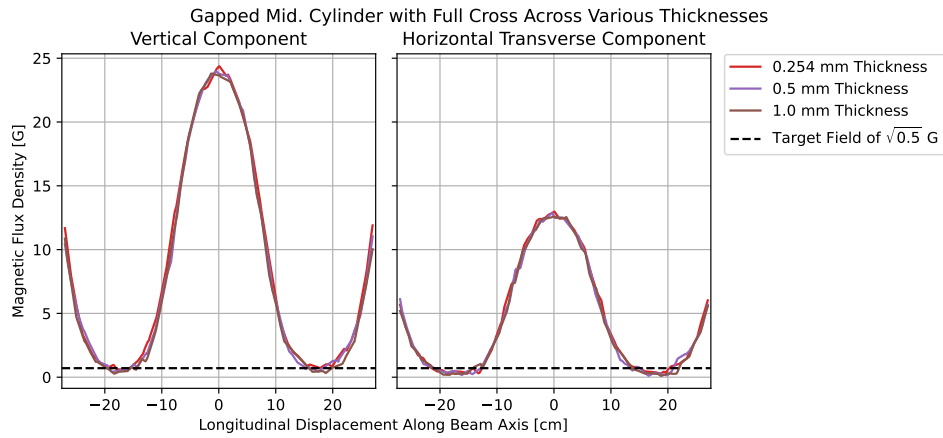
Simple Compensation: A. Solid Cylinder



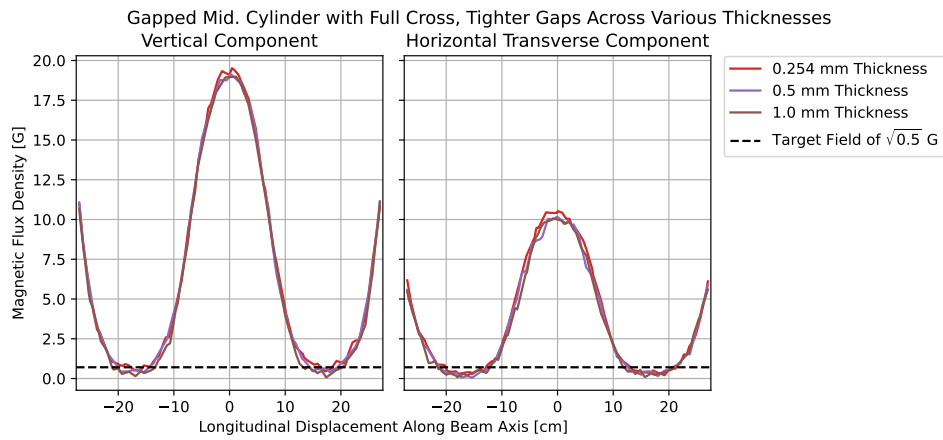
Diagnostic Box: B. Gapped Middle Cylinder



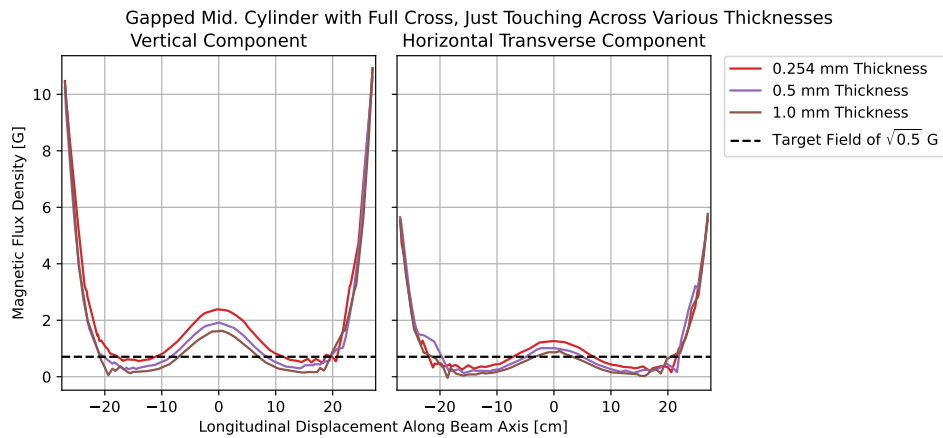
Diagnostic Box: C. Full Cross



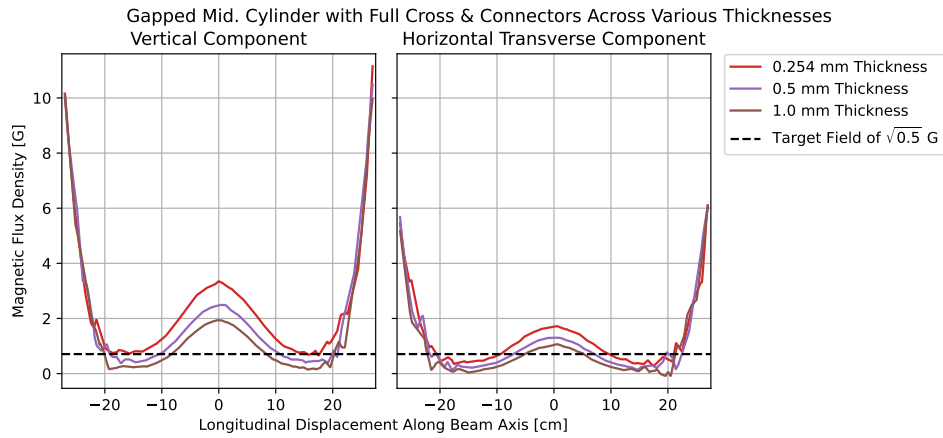
Diagnostic Box: D. Full Cross with Smaller Gaps



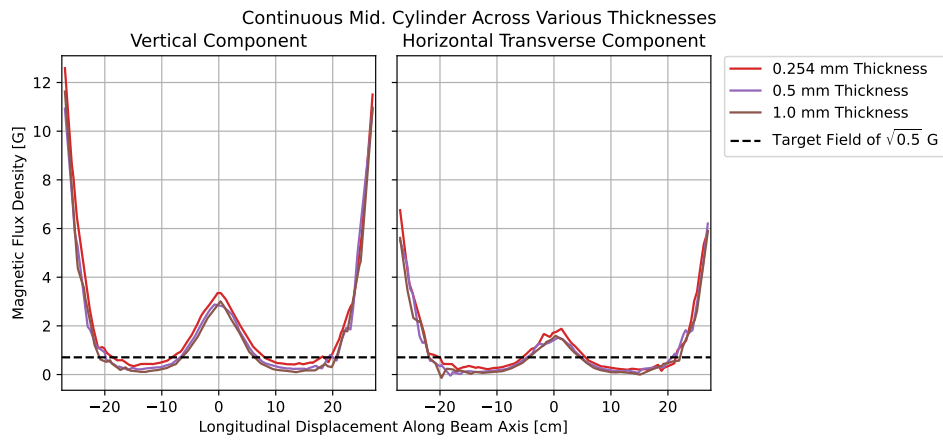
Diagnostic Box: E. Full Cross, Just Touching



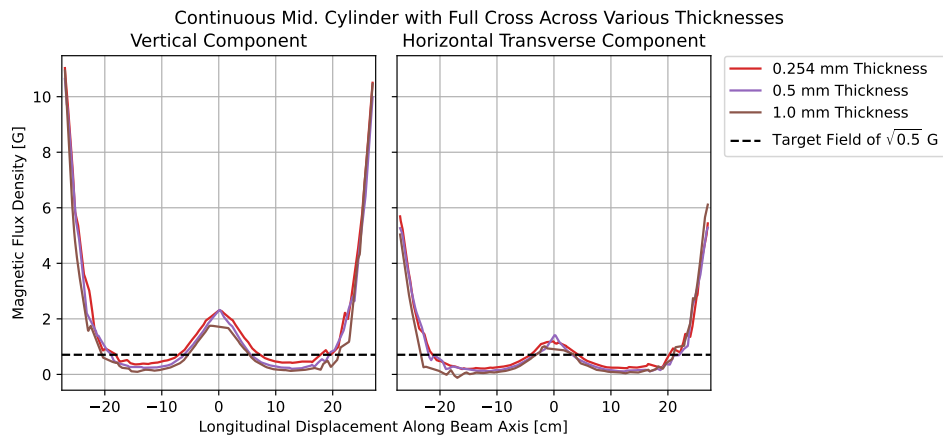
Diagnostic Box: F. Full Cross with Connectors



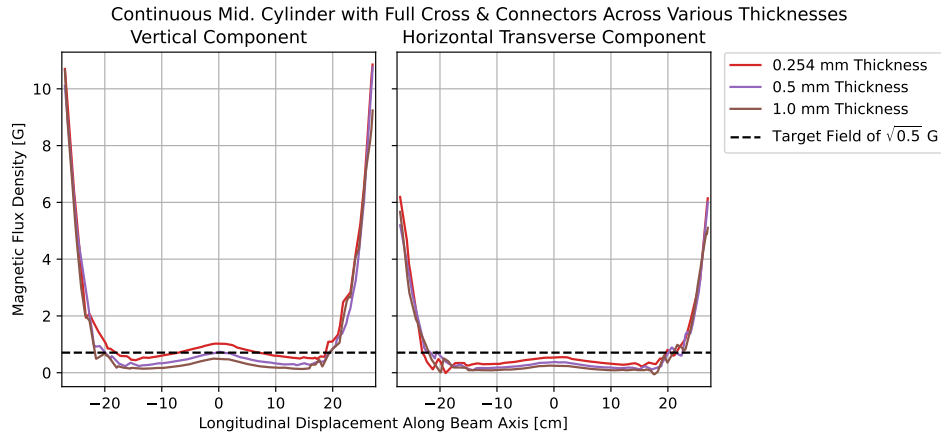
Diagnostic Box: G. Continuous Middle Cylinder



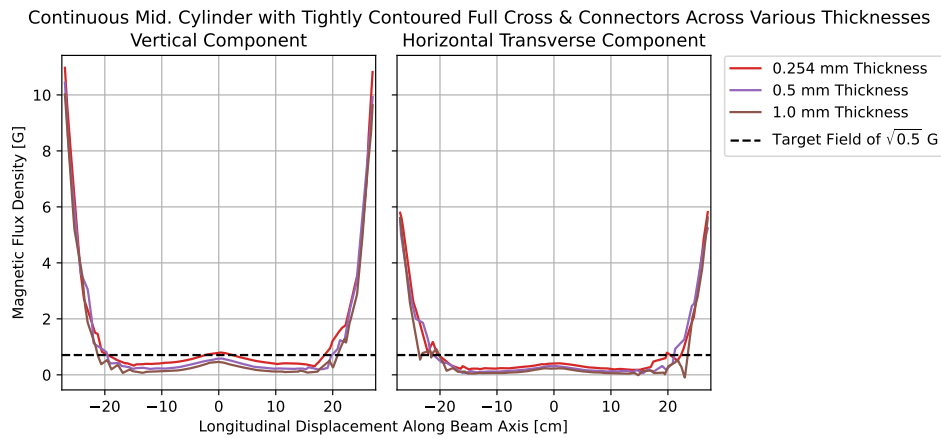
Diagnostic Box: H. Continuous Middle Cylinder with Full Cross



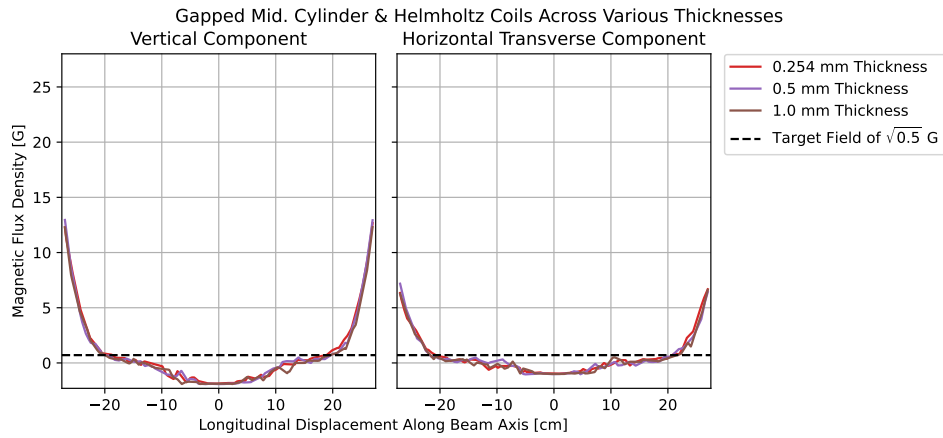
Diagnostic Box: I. Continuous Middle Cylinder with Full Cross and Connectors



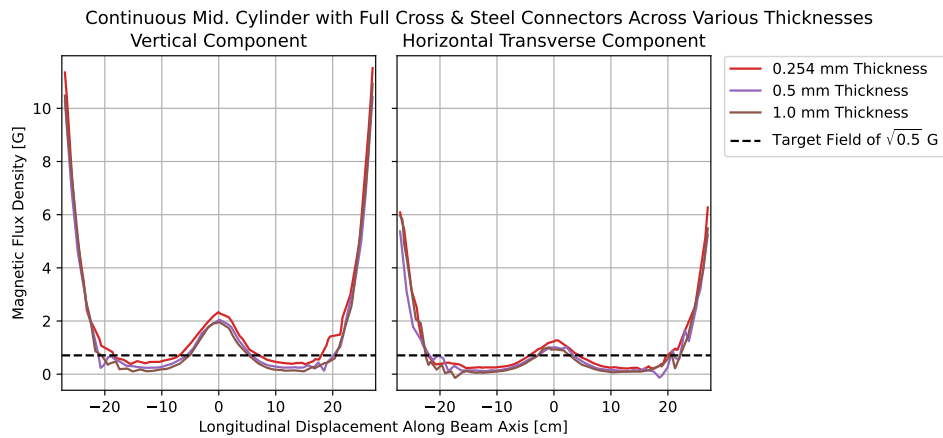
Diagnostic Box: J. Tightly Contoured Continuous Middle Cylinder with Full Cross and Connectors



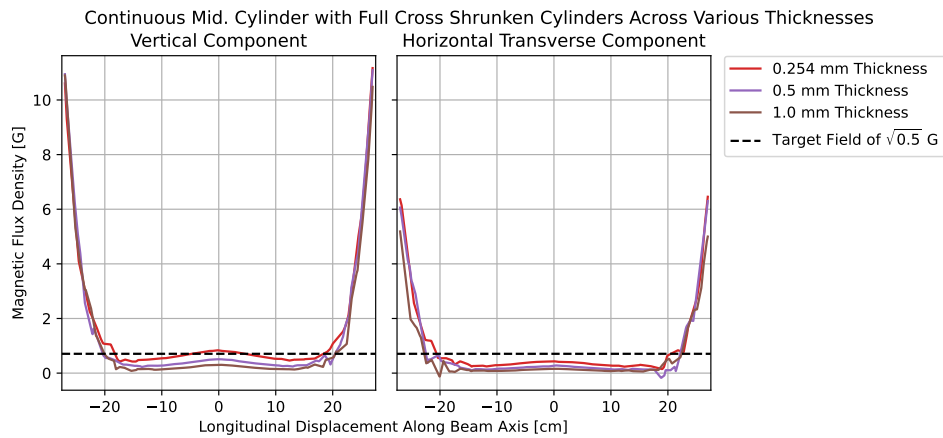
Diagnostic Box: K. Active Cancellation



Diagnostic Box: L. Mild Steel Connectors



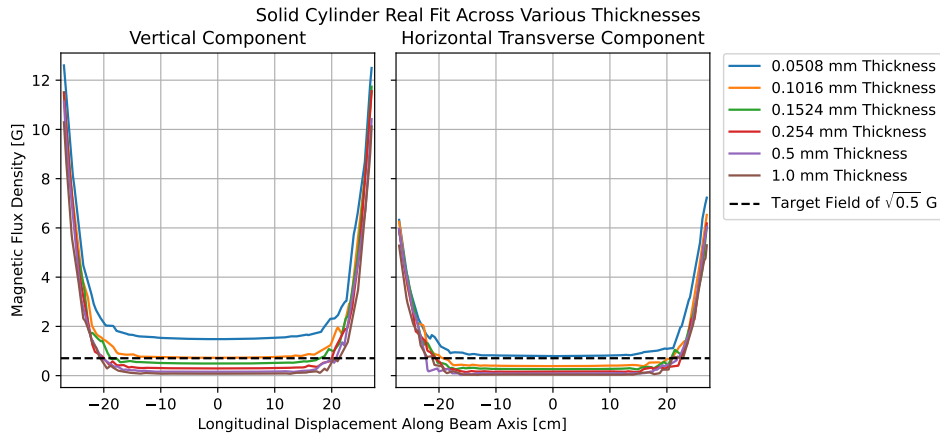
Diagnostic Box: M. Shrunken Aperture



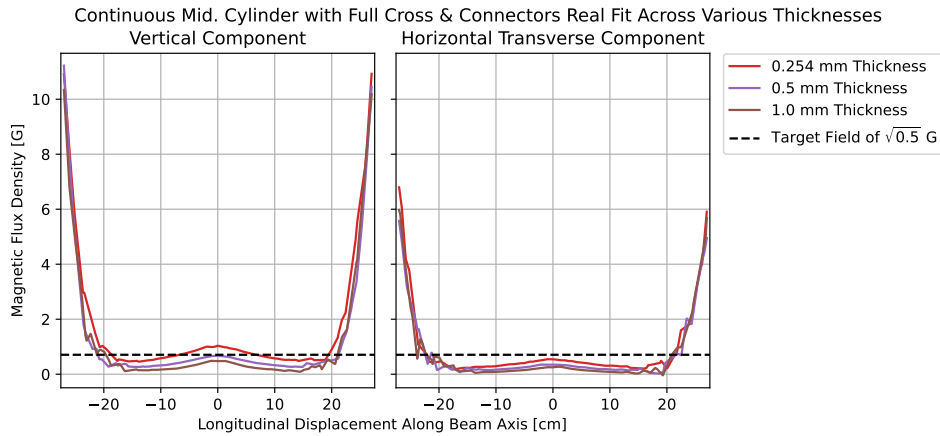
5.4 Optimal Configurations Reduced Radius to 7.006 cm for Real Fit

The reduced radius variant of the 3 optimal configurations all show slightly improved shielding effectiveness compared to the individual non reduced radius versions of the configurations of appendix 5.3. The reduced radius is set at 7.006 cm such that it allows spacing between the beam component wall and itself, and also leaves equal spacing between it and the electrostatic quad of ART0268¹¹, preventing virtual leaks and preventing interference with electrostatic steering.

Simple Compensation: A. Solid Cylinder Real Fit

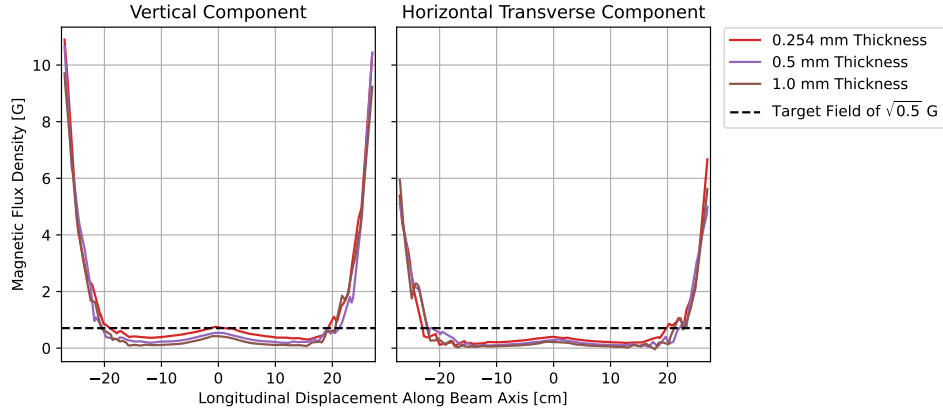


Diagnostic Box: I. Continuous Middle Cylinder with Full Cross and Connectors



Diagnostic Box: J. Tightly Contoured Continuous Middle Cylinder with Full Cross and Connectors

Continuous Mid. Cylinder with Tightly Contoured Full Cross & Connectors Real Fit Across Various Thicknesses



5.5 Chained Configuration

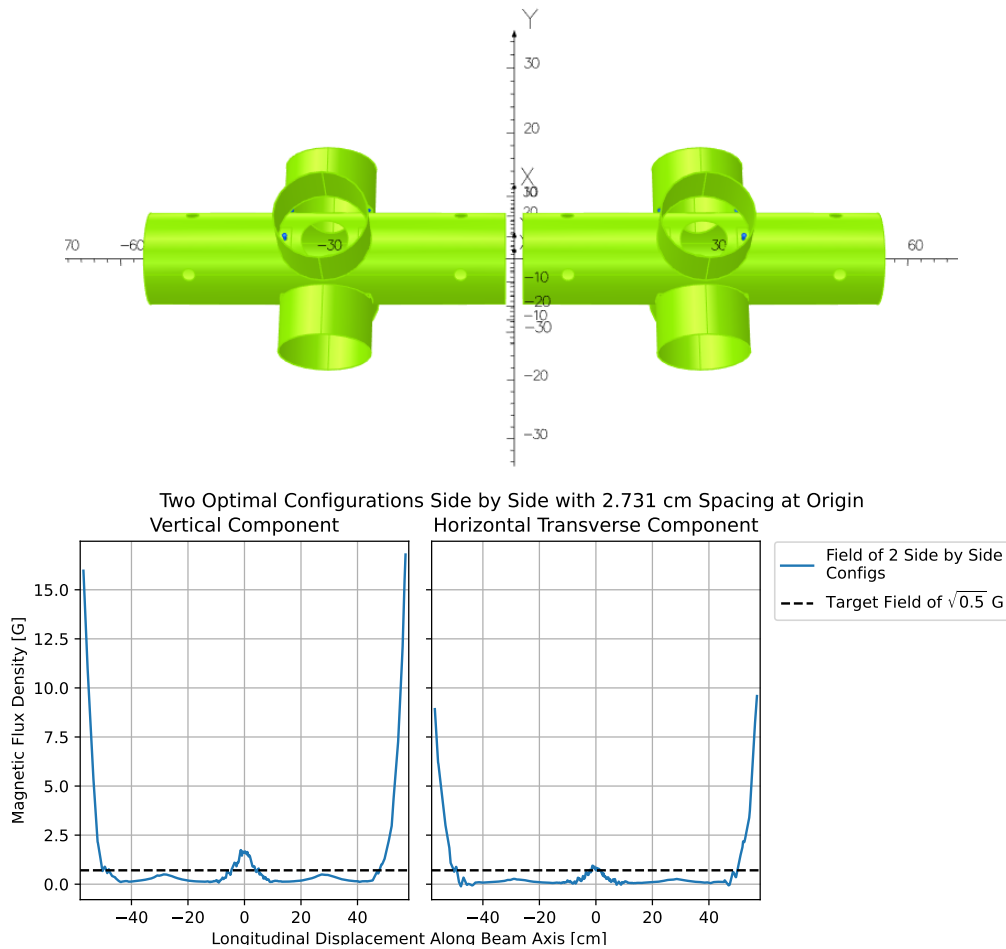


Figure 34: OPERA simulation geometry and post analysis on-axis field data for two optimal configurations (config I) placed side by side, a potential layout placement for the real horizontal section replacement as shown by the side by side diagnostic boxes in ART0052¹². The gap between the two configurations is to accommodate the outer flanges of the electrostatic quadrapoles between the 2 side by side diagnostic boxes which from ART0052¹² measures to 1.731 cm, with an additional 0.5 cm on each side for clearance. The data shows that despite the gap, the magnetic field is not extremely high, being very close to target field. This represents a primitive analysis of multi configuration analysis, which has further experimentation suggested in the suggestions subsection of the compensation configurations section.

5.6 Directory and File Descriptions

The main file directory contains 5 main sub directories: 1) Analysis Code, which contains the code for all data processing and visualization, 2) Data, which contains all collected data and outputted processed data, 3) Measurement Jig, which contains all CAD construction files, pictures, and measurements for the tripod measurement jig, 4) OPERA files, which contains all .opc, .op3, .bh, and other files for the compensation configurations section, and 5) Pictures and Plots, which contains the outputted data visualizations and various other pictures used in this report. Relevant notebooks and directories under the Analysis Code, Data, and OPERA files directories will be given further brief description. The files of Measurement Jig and of Pictures and Plots are easier to understand from file names, and do not require further description.

Analysis Code/Cyclotron Main Survey and Axially Symmetric Measurements.ipynb

IPython notebook containing the data processing and visualization for most of the stray field mapping section data including the main survey data processing and visualization, main stray field mapping extrapolations calculations and visualization, the axially symmetric confirmation measurements' processing and visualization, the theoretical expectation calculation and visualization, and miscellaneous magnetic field peak finding plots.

Analysis Code/stray field mapping/I2 Analysis Rough 2D.ipynb

IPython notebook containing the data processing and visualization for the on-axis and off-axis rough measurements of the open part of I2's north-south seen in appendix 5.1.

Analysis Code/compensation configurations/Mu-metal Compensation Configuration Comparison.ipynb

IPython notebook containing the data processing and visualization for most of the compensation configurations section, including the processing and visualization for the comparison of all compensation configurations at 1 mm thickness, and the processing and visualization for each individual configuration at the various thicknesses tested, including the reduced radius real fits of appendix 5.4.

Analysis Code/compensation configurations/Misc Cross Shielding Analysis.ipynb

IPython notebook containing processing and visualization for the generic mu-metal and CryoPerm bh curve comparison of appendix 5.2 and processing and visualization for the chained optimal configurations of appendix 5.5.

Analysis Code/compensation configurations/Mock-up Measurement Analysis.ipynb

IPython notebook containing processing and visualization for the mu-metal mock up measurements of the Configuration Physical Mock-up Measurements subsection of the compensation configurations section.

Data/stray field mapping/main survey

Directory containing data related to the main stray field measurements survey and processing. The raw data sub-directory contains the raw measurements of magnetic field with onaxis.csv containing the on-axis measurements of the open section further down the horizontal section and offaxis.csv containing the rest of the indirect off-axis measurements. The data sub-directory contains the processed version of this data, with the axes corrected to point in the direction given in this report. The extrapolated data sub-directory includes the map given by each of the 7 simple extrapolation methods attempted with the 2 best from the stray field mapping section being “Mean of Possible Furthest 3.csv” and “On-axis Set as Furthest Data.csv”.

Data/stray field mapping/axially symmetric

Directory containing data related to the axially symmetric confirmation measurements, with similar “raw data” and “data” folders as the main survey directory. The data recording sheets directory contains the excel sheets which contain the calculated Cartesian points for the 110.5 degree symmetric tape line in CalculationOfXYCoords.xlsx and the points measured at with the tripod jig offset in AxiallySymmetricMeasurementSheet.xlsx.

Data/stray field mapping/rough I2

Directory containing .csv data of the rough I2 measurements, split into 3 csvs for each of the 3 components of magnetic field.

Data/stray field mapping/mockup data

Directory containing data related to the mock up measurements of the compensation configurations section, with similar “raw data” and “data” folders as the main survey directory. The unshielded.csv file is the measurement of background field on the shielding configuration axis, and the shielded.csv file is the measurement of shielded field on the shielding configuration axis, within the mu-metal mock-up. Also contained is a sub-directory named “nonlinear sim” containing primitive non-linear simulation data and OPERA files for the mock-up subsection.

Data/compensation configurations

Each individual indexed directory in this folder contains all the on-axis buffer data for a particular compensation configuration analyzed. 0 is config A, 0.1 is the reduced radius config A, 3 is config B, 4 is config K, 5 is config C, 6 is config D, 7 is config E, 8 is config F, 10 is config G, 11 is config H, 12 is config I, 12.1 is the reduced radius config I, 13 is config L, 14 is config M, 15 is config J, and 15.1 is the reduced radius config J. Index 1, 2, and 9 are not discussed in this report, but contain other configurations examined during simulation work. The indexed directories each contain csvs of buffer data, with the particular csv’s file name giving the metal thickness examined for that file and the bh curve used. Also contains the directory side by side, which contains the buffer data for appendix 5.5.

OPERA files/bh curves

Directory containing the CryoPerm and Generic Mu-metal BH curves.

OPERA files/constant field shielding

Directory containing all of the .opc and .op3 OPERA simulation geometry and post processed data files, with the exact same organization and naming scheme as the

Data/compensation configurations directory. The constantfield120percentmaxofaverage.xml file is the constant external magnetic field described in the compensations configurations section, used for the analysis of all these files.

OPERA files/mockup files

Directory containing the STL geometry and picture for the mock up, of the mock up confirmation measurements of the compensation configurations section.

OPERA files/step wise field compensation testing

Directory containing all previous work in non constant field configuration testing. Briefly the idea was to use chained rectangular coils, generating fields in the two transverse directions, to create a step wise field on and nearby the axis, with each step's magnetic field magnitude and direction being the corresponding transverse component value of the stray field map. The configuration or multiple configurations could then be put inside the middle of the sequence of coils, experiencing the changing of the magnetic field seen in the stray field mapping. Ahrendsen et al.¹³ were useful resource for rectangular coil spacing, for this experimental work.